

Macroscopic and mesoscopic characterization of a bistable reaction system: CO oxidation on Pt(111) surface

Martin Berdau,^{a)} Georgii G. Yelenin,^{b)} Andrzej Karpowicz,^{c)} Mohammad Ehsasi, Klaus Christmann,^{d)} and Jochen H. Block^{a),e)}

Freie Universität Berlin, Institut für Physikalische und Theoretische Chemie, Takustrasse 3, D-14195 Berlin-Dahlem, Germany

(Received 24 April 1998; accepted 17 March 1999)

The catalytic oxidation of CO by oxygen on a platinum (111) single-crystal surface in a gas-flow reactor follows the Langmuir–Hinshelwood reaction mechanism. It exhibits two macroscopic stable steady states (low reactivity: CO-covered surface; high reactivity: O-covered surface), as determined by mass spectrometry. Unlike other Pt and Pd surface orientations no temporal and spatiotemporal oscillations are formed. Accordingly, CO+O/Pt(111) can be considered as one of the least complicated heterogeneous reaction systems. We measured both the macroscopic and mesoscopic reaction behavior by mass spectrometry and photoelectron emission microscopy (PEEM), respectively, and explored especially the region of the phase transition between low and high reactivity. We followed the rate-dependent width of an observed hysteresis in the reactivity and the kinetics of nucleation and growth of individual oxygen and CO islands using the PEEM technique. We were able to adjust conditions of the external control parameters which totally inhibited the motion of the reaction/diffusion front. By systematic variation of these conditions we could pinpoint a whole region of external control parameters in which the reaction/diffusion front does not move. Parallel model calculations suggest that the front is actually pinned by surface defects. In summary, our experiments and simulation reveal the existence of an “experimental” bistable region inside the “computed” bistable region of the reactivity diagram (S-shaped curve) leading to a novel dollar (\$) shaped curve. © 1999 American Institute of Physics. [S0021-9606(99)70122-4]

I. INTRODUCTION

The research area concerned with the dynamical behavior of open nonequilibrium systems in physics, chemistry, reactor technology or biology has grown during the last two decades to an exciting and productive part of natural sciences, and one is very much interested in mutual correlations or universal behavior of the respective systems.^{1–4} From the chemical point of view, “simple” (two-dimensional) surface reactions such as the catalytic oxidation of carbon monoxide belong to a class of systems whose dynamical behavior is still relatively transparent compared with the well-known three-dimensional solution reactions of the Belousov–Zhabotinskii type,^{5,6} which are considerably more complicated. Much effort has been devoted to elucidate the dynamical properties of the catalytic CO oxidation on platinum metal surfaces. Accordingly, there exists a real wealth of literature about, among others, hysteresis phenomena, kinetic oscillations, or pattern formation during the catalytic CO ox-

idation on various metal single-crystal surfaces.⁷ Nevertheless, only part of the actual physical surface processes is really understood, the reason being that the elementary steps are influenced by a whole variety of specific microscopic and mesoscopic details which are not very well known in all cases. For example—and this will be shown in the present work—mesoscopic crystallographic surface defects must be reckoned among these unknown “details” which may introduce a certain degree of “noise” to the body of external control parameters and assist, for example, nucleation phenomena or cause a pinning of reaction/diffusion fronts in a given pressure range.

It is convenient to distinguish the true *microscopic* range, with length scales $1 \leq \lambda \leq 1000$ nm, from the *mesoscopic* ($1 \leq \lambda \leq 1000$ μ m) and *macroscopic* range ($\lambda > 1$ mm), because different physical phenomena are imaged by the available microscopies or surface-analytical techniques: In the *microscopic* regime, coverage-dependent surface reconstructions and/or order–disorder phase transitions within the adsorbed phase(s) can occur during the reaction and have indeed been observed by scanning tunneling microscopy (STM) or low-energy electron diffraction (LEED).^{8,9} On the *mesoscopic* scale, spatiotemporal oscillations like target patterns, spirals, standing waves, chemical turbulence, and solitary waves have been found for several Pt metal surfaces using photoelectron emission microscopy (PEEM).¹⁰ The extension of these phenomena into the atmospheric pressure regime could recently be followed by opti-

^{a)}Also at Fritz-Haber-Institut der Max-Planck-Gesellschaft, Abteilung Grenzflächenreaktionen, Faradayweg 4-6, D-14195 Berlin-Dahlem, Germany.

^{b)}Also at Moscow State University, Department of Computational Mathematics and Cybernetics, Laboratory for Mathematical Modeling in Physics, Vorobjevi Gori, 119899 Moscow, Russia.

^{c)}On leave from Technical University of Wrocław, Wybrzeże Wyspińskiego 27, 50-370 Wrocław, Poland.

^{d)}Electronic mail: kchr@chemie.fu-berlin.de

^{e)}Deceased.

cal microscopies, namely, ellipsometric microscopy for surface-imaging (EMSI) and reflection-anisotropy microscopy (RAM).¹¹ Furthermore, the *macroscopic* regime can be investigated by more conventional methods like work function change ($\Delta\Phi$) and reaction rate measurements which probe the “integral” behavior of the respective system.

Dynamical phenomena that lead to the formation of the aforementioned temporal or spatiotemporal oscillations (see Ref. 12 for definitions), have been reported for the O-mediated CO oxidation on Pt(100),^{9,13} Pt(110),^{14,15} Pt(210),^{12,16,17} as well as on Pd(110) surfaces,¹⁸ and for NO-mediated CO oxidation on Pt(100).^{19,20} A great deal of further experimental and theoretical work is aimed at an understanding of the complicated oscillatory phenomena.^{7,21–27}

Among all these reaction systems with their fairly complex dynamical behavior the CO+O/Pt(111) system is somewhat exceptional, because it does not show any spatiotemporal oscillations commonly observed with crystallographically open Pt surfaces. On the macroscopic scale, the system only exhibits two stable steady states, namely, a state of low reactivity with a predominantly CO covered surface, and a state of high reactivity with a largely oxygen-covered surface. Transitions between these two states are, of course, possible and manifest themselves in a hysteresis, if an external control parameter, e.g., the CO partial pressure, is varied back and forth. Phenomenologically, the width of the hysteresis loop depends to some extent on the scan rate $\beta_{CO} \equiv dP_{CO}/dt$ in a way that a smaller β_{CO} reduces the width of the loop. At this point a principal question arises, namely, whether or not this width approaches and reaches even zero for an infinitely low scan rate. This is equivalent to the problem of whether a region of bistability between the two *stable* steady states exists, which will be a major issue of the present paper.

Previous experimental and theoretical work for CO oxidation on Pt(111) has been surveyed in a recent review article by Zhdanov and Kasemo.²⁴ On the theoretical side, the mathematical model and simulations are based upon a system of nonlinear partial differential equations that follow from the common Langmuir–Hinshelwood (LH) reaction mechanism,^{9,25,26} assuming coadsorption of both CO (one adsorption site required) and oxygen during the reaction (two adjacent sites required, a condition introduced by the necessary dissociation of the oxygen molecule).

Based on the elementary LH reaction steps, different models can be applied to simulate the surface-chemical situation and to predict both the macroscopic and mesoscopic dynamical behavior of the system. These models can be distinguished by their level of sophistication, and the principal features of three important levels of simulation (a)–(c) are schematically illustrated in Fig. 1. Shown is a column of three associated plots of a state variable (such as the macroscopic stationary CO coverage Θ_{CO} (y coordinate) against a decisive control parameter [the “CO partial pressure,” p_{CO} (x coordinate)], while all other control parameters are kept constant. Both the coverage and distribution of the reactants CO and oxygen respond directly to the adjustment of an external control parameter (flow rate F , CO and O₂ partial pressures, sample temperature T , scan rates β_i of tempera-

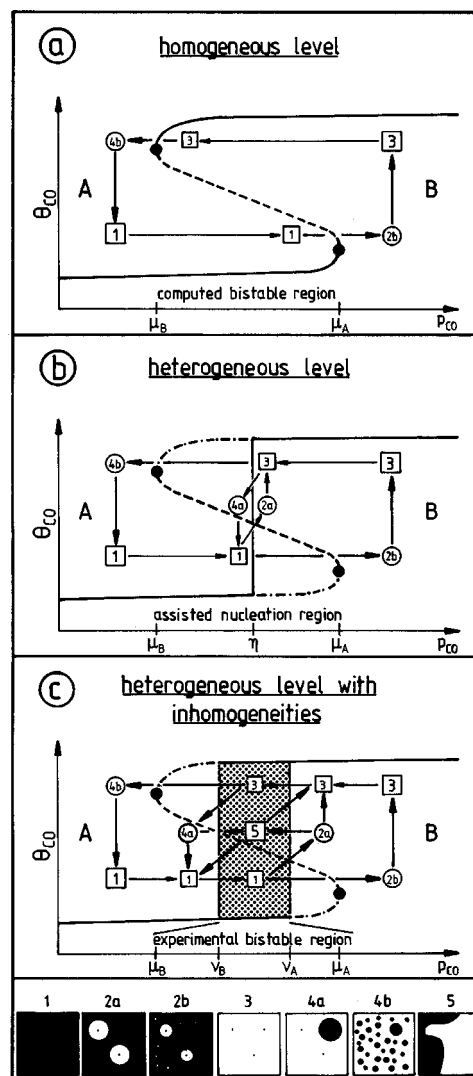


FIG. 1. A “nonlinear bistable system” is characterized by the dependence of a state variable (the CO coverage Θ_{CO}) on a control parameter (the CO pressure) and result in a typical S-shaped curve (a) or in our new $\$$ -shaped curve (c). The two experimentally relevant steady states of high reactivity (low Θ_{CO}) and low reactivity (high Θ_{CO}) can either be stable (solid line) or metastable (dash-dotted line); the third state is unstable (dashed line) and occurs only in simulations. The stripe of schematical PEEM patterns in the bottom illustrates the principal mesoscopic features observable on the surface. *Macroscopic* states are indicated by squares and circles, whereby we delineate *stable* states by squares, and *transient* states by circles. (in the text, we denote the “square” states by braces and the “circle” states by round brackets). Summarized are three levels of deterministic modeling (all resting upon the Langmuir–Hinshelwood reaction steps (a)–(c)). (a) Simulations based on the homogeneous level considering only the ordinary differential equations of the LH reaction steps and resulting in a simple S-shaped curve. The possible macroscopic steady states can be either stable (solid lines) or unstable (dashed line). The two bifurcation points μ_A and μ_B separate the (computed) bistable region from the two monostable regions A and B. (b) Simulations based on the heterogeneous level with diffusion terms added to the differential equations of the homogeneous model: For a certain CO partial pressure, an equistability point η inside the computed bistable region results. A region of assisted nucleation of CO ($\eta < p_{CO}$) and oxygen islands ($\eta > p_{CO}$) consisting of initial supercritical nuclei appears within the computed bistable region due to high noise level. For extremely slow scans of p_{CO} the macroscopic hysteresis degenerates to a single transition right at the equistability point η . (In the absence of noise the model gives the same width of hysteresis loop as the above-mentioned model of homogeneous level). (c) Simulations based on the *heterogeneous level with inhomogeneities* do consider defects. A so-called dollar- ($\$$ -) shaped curve is obtained, whose prominent feature is the additional region of experimental bistability inside the region of assisted nucleation. Both regions are separated from each other by the points ν_A and ν_B .

ture, CO and oxygen pressure, respectively) and monitor the state of the system. A very useful and convenient probe for the lateral distribution of the reactants on the mesoscopic scale is the already mentioned PEEM technique, and accordingly, we add to the bottom of Fig. 1 a stripe containing a sequence of schematic patterns (denoted 1–5) which can be observed by PEEM and define the various mesoscopic “states” of the reacting system. Figures inside a square denote *stable* states, while figures inside the circles mark *spatiotemporal* (i.e., transient) patterns formed on the surface during transition between stable states. [Concerning the PEEM contrast, we recall that the CO-covered Pt(111) surface exhibits a low work function and produces *bright* PEEM images, while an O-covered Pt(111) surface with its higher work function causes a *dark* PEEM image].

The three diagrams of Fig. 1 describe the principal possibilities of how a nonlinear reaction system can be classified. The typical S-shaped curve shows three steady states of reactive behavior, which are either stable (solid line), metastable (dash-dotted line), or unstable (dashed line). The *unstable* steady state is only mathematically relevant and will be neglected in the following. The remaining two steady states are then either stable or metastable. Turning to the special case of CO oxidation, we have (altogether two) stable steady states represented by the oxygen-covered surface (the lower branch of the S-shaped curve at low CO coverage Θ_{CO}) and by the CO-covered surface (the upper branch of the S-shaped curve at high Θ_{CO}), respectively. Since the oxygen-covered surface exhibits a high reactivity, we denote the respective state as the *steady state of high reactivity* or simply the *oxygen side*. In contrast, the reactivity of the CO-covered surface is low and we refer to it as the *steady state of low reactivity* or simply the *CO side*. Apparently, the control parameter (in our case the CO pressure) is the crucial quantity that determines the stability of a state and its location in reactivity space. For the following consideration it is convenient to introduce boundary values called μ , ν , or η . In all three levels of the LH model [Figs. 1(a)–1(c)] the system resides in the steady state of high reactivity within the monostable region A, if $p_{\text{CO}} < \mu_B$, but it will reside in the steady state of low reactivity (within the monostable region B) if $p_{\text{CO}} > \mu_A$. Interestingly, for the interval $\mu_B < p_{\text{CO}} < \mu_A$ the final “state” of the system depends on history, i.e., which monostable region the variation of the control parameter is started from. How well the experimental behavior of the system is simulated or theoretically predicted depends sensitively on the degree of sophistication of the mathematical modeling. Actually, this level of modeling can reveal quite a complicated dynamic behavior of the system, resulting also in a more complex structure of the S-shaped curve as evident from Figs. 1(b) and 1(c). The three levels of simulation mentioned above can be characterized as follows:

(a) The *homogeneous* level considers only the ordinary differential equations that describe the LH reaction steps, while diffusion terms and surface defects are completely neglected. On this (fairly crude) level, merely the *macroscopic* behavior of the system can be predicted. Nevertheless, it is interesting to note that—although one departs from an initially spatially absolutely homogeneous and defect-free

configuration—monostable and bistable regions occur for certain combinations of the control parameters. Upon variation of a single control parameter, a simple S-shaped curve represents the possible macroscopic steady states. These can be mathematically either stable [solid lines in Fig. 1(a)] or unstable [the dashed line in Fig. 1(a)]. In other words, the system will have to “decide” between one of the two stable steady states, if the control parameter (e.g., the CO partial pressure) is adjusted between the two (indicated) bifurcation points μ_A and μ_B . For convenience and clarity, we denote this bistable area as the *computed bistable region*. In the frame of this simple deterministic description the width of the hysteresis loop equals the width of the computed bistable region.

(b) On the *heterogeneous* level only diffusion terms are added to the differential equations of the homogeneous model. Still, defects are not considered. This simulation can successfully model the shape of the initial critical nuclei, the regions of assisted nucleation of CO- and oxygen states, and the equistability condition. Furthermore, it is helpful to investigate the initial growth of supercritical nuclei of both CO and oxygen during the transition between the two steady states and the disappearance of subcritical nuclei. We emphasize, however, that this deterministic mesoscopic model is unable to explain the nucleation of a new state.

(c) The most far-reaching deterministic model, viz., the *heterogeneous level with inhomogeneities*, departs from the heterogeneous level, but no longer excludes defects. Only this model allows us to investigate the appearance of a nucleus of new state in the vicinity of a local surface defect. The resulting prominent new feature is the additional *region of experimental bistability* inside the region of assisted nucleation. *Both* regions are separated from each other by the points ν_A and ν_B . Accordingly, the macroscopic and mesoscopic behavior of the reactive system is strongly affected and deviates substantially from the predictions of the two other models (a) and (b).

We have a closer look at the *heterogeneous* level (b) and refer to the middle part of Fig. 1. We realize that there now occurs an equistability point η at a critical CO partial pressure where the respective macroscopic stable steady state becomes metastable (indicated by the dash-dotted lines). Consequently, either CO (if $p_{\text{CO}} > \eta$) or oxygen islands (if $p_{\text{CO}} < \eta$) can form as supercritical initial nuclei in the aforementioned computed bistable region. As p_{CO} approaches the equistability point η the size Δ of a critical initial nucleus increases; directly at η , Δ becomes infinite. Hence, to initiate the growth of a new state in close vicinity to η , a large initial fluctuation is required. In order to distinguish the computed bistable region occurring in this model (c) from the computed bistable region of the homogeneous model (a) we call it the *region of assisted nucleation*. This region contains the subregions of assisted nucleation of the *CO state* ($\eta < p_{\text{CO}} < \mu_A$) and of the *oxygen state* ($\mu_B < p_{\text{CO}} < \eta$). Outside this region, adsorbing CO ($p_{\text{CO}} > \mu_A$) or adsorbing oxygen molecules ($p_{\text{CO}} < \mu_B$) nucleate spontaneously and rapidly, and accordingly, we denote the respective ranges in reactivity space as regions (A or B) of spontaneous nucleation.

Zhdanov and Kasemo²⁴ concluded that the macroscopic

hysteresis will vanish, if the islands nucleate and grow sufficiently rapidly. In other words, a steplike change of the reactivity (and coverage) at a single decisive CO partial pressure is predicted which is equivalent to the aforementioned equestability point η of the two phases, where the hysteresis loop degenerates to a single line. Of course, the aforementioned growth velocity has to be considered more closely: The average time t required for the spontaneous formation of a supercritical fluctuation is proportional to $\Delta^{2/3} \exp(a\Delta^2)$, with the constant $a > 0$.⁴⁸ In close vicinity to η (see above), t may be orders of magnitude greater than the period of even a slow p_{CO} -scan experiment. Consequently, a finite hysteresis loop may be found even in this case of an extremely slow p_{CO} scan. Despite this reservation, the main conclusion about the disappearance of a hysteresis remains valid, if the system exhibits a rather high noise level. Noise here means uncertainties and fluctuations of the decisive external control parameters. Bär *et al.*,²⁷ using the same model, combine the condition of equestability and island growth when they state that the *front velocity* of the island growth reaches zero right at the equestability point.

In order to understand the system's *lateral* response to deliberate variations of a control parameter we perform a cyclic variation of the CO partial pressure and start off with the oxygen-covered state¹ of high reactivity in the area of the monostable region A. Please note that figures inside braces symbolize *stable* states while figures inside round brackets denote *spatiotemporal* states. The associated surface morphology is a plain surface covered exclusively with oxygen (black area {1} in the sequence of schematical PEEM images at the bottom of Fig. 1). Following the arrow to the right [Fig. 1(b)], the points η and μ_A are reached and crossed. The following behavior depends crucially on the scan rate β_{CO} . For high β_{CO} , p_{CO} is driven rapidly into the region of spontaneous nucleation beyond μ_A , and one observes rapid nucleation and subsequent growth of *small* CO islands in an oxygen environment [“white” spots or nuclei in a dark “sea” of adsorbed oxygen, cf. pattern 2(b)]. For small β_{CO} , on the other hand, the system first remains inside the region of assisted nucleation for a long time, and large CO islands [shown in Fig. 2(a)] can develop and finally cover the entire surface (except some defects). Finally, however, the system approaches and transforms to the *stable* steady state of low reactivity (the CO-covered surface), and pattern {3} is obtained. If the CO partial pressure is now gradually reduced [Fig. 1(b)], the system remains in the (*metastable*) steady state of low reactivity for a whole while, even though point η is crossed again. In a similar manner as formerly described for positive β_{CO} , the transition to the steady state of high reactivity takes place via nucleation and growth of “dark” oxygen islands in a “white” surrounding of CO adsorbate, the details depending on the scan rate β_{CO} . Pattern 4(a) is observed for slow scan rates, while pattern 4(b) is characteristic of spontaneous nucleation of many small oxygen islands within a “sea” of CO adsorbate at high negative values of β_{CO} . Finally, the initial situation, namely the highly reactive oxygen-covered surface {1}, is restored and the cycle completed.

In the following work we will focus, by *experimental*

means, but also supported by model simulations taking care of *defects*, on exactly these two conclusions about a vanishing macroscopic hysteresis and the lateral mesoscopic morphology and its dynamic behavior in the critical regime of computed bistability. We will especially investigate the effect of the scan rate β of an external control parameter on the macroscopic reaction rate by following the hysteresis loop as a function of β , and by directly watching the (mesoscopic) island growth by means of PEEM. The *macroscopic* measurements will be dealt with in Sec. III A, while data about the lateral *mesoscopic* behavior are presented in Sec. III B. We will deduce that—despite Zhdanov's and Kasemo's predictions²⁴—a finite experimental hysteresis loop does exist which in turn proves the existence of a true region of experimental bistability (between two *stable* steady states).

Our experiments and model simulation (*heterogeneous level including defects*) enable us to construct the more sophisticated (but realistic) reactivity diagram presented in Fig. 1(c) which we call, for simplicity, the dollar-shaped curve. It is a consequence of the consideration of defects and characterized by the appearance of an experimental bistable region inside the area of assisted nucleation as indicated in Fig. 1(c). In this particular region the system stays in either one of the two *stable* steady states, and a special adjustment of the experimental parameters will drive the system into stationary behavior with neighboring CO and oxygen areas, indicated in Fig. 1(c) as state {5}. On various occasions, we will return to Fig. 1(c) in our paper.

II. EXPERIMENT

All experiments were carried out in a 30 cm stainless steel ultrahigh vacuum reaction chamber (base pressure in the low 10^{-10} Torr range) equipped with a mass spectrometer and a photoelectron emission microscope (PEEM), besides the standard facilities to clean and characterize a metal single-crystal surface. As described elsewhere,²⁸ PEEM provides a magnified image of the surface, due to the work-function-induced intensity contrast of the photoelectrons emitted from the surface after irradiation with UV light.

The platinum (111) sample was x-ray oriented and cut to within 0.5° from a high-purity (5N) single-crystal boule; its effective area was 66 mm^2 . Appropriate cleaning was accomplished using repeated cycles of Ar^+ ion sputtering, followed by gentle treatments in oxygen. By means of a PID regulator, the sample temperature could be adjusted and kept constant to within $\pm 0.1 \text{ K}$. The partial pressures of CO and oxygen (O_2) were measured by means of a Bayard–Alpert-type ion gauge in the pressure regime $10^{-10} \text{ Torr} < p_i < 10^{-5} \text{ Torr}$ (total error $\sim 20\%$), and by a spinning-rotor gauge for $p_i > 10^{-6} \text{ Torr}$ (total error $\sim 3\%$). A sophisticated gas purification and inlet control system allowed us to keep the gas pressures strictly constant, to program linear positive or negative pressure rises, or to perform pressure jumps (maximum regulation time 10 s). Due to the electronic regulation (Stange Micro-programmer SE-131-N) pressure changes within an accuracy of 1% of the set value could be routinely performed. The pumping speed could be determined independently and regulated by a standard gate valve. Before use,

the already very clean gases (CO: 99 997 vol %, Linde; oxygen: 99 999 vol %, Linde) were further purified with the help of special zeolite molecular sieves.

We judged the reactivity of the Pt(111) surface from the CO₂ mass spectrometer signal (amu 44). A (qualitative) measure of the CO and oxygen coverages is provided by the work function of the sample as monitored by PEEM (here, a circular area of 380 μm in diameter is imaged). For Pt(111), the final work function produced by a saturation coverage of oxygen²⁹ seems to be significantly higher than the work function caused by CO;³⁰ accordingly, islands of adsorbed oxygen appear dark (low photocurrent) while islands of carbon monoxide are bright (large photocurrent). The PEEM images were recorded by a charge-coupled device (CCD) camera and stored on a HI-8 video tape (full-frame image 40 ms, half-frame image 20 ms); a special computer program allowing image averaging (the presented images consist of 2–10 video frames) helped considerably to reduce the image noise. It also enabled us to take difference images and to observe and judge slow changes in the morphology of the surface.

III. RESULTS

A. Macroscopic behavior

1. Influence of external control parameters

Figure 2 shows the crude macroscopic behavior of a Pt(111) single-crystal surface held at a temperature $T = 413.2$ K and exposed to a constant oxygen partial pressure ($p_{O_2} = 4 \times 10^{-5}$ Torr), while the CO partial pressure is varied (at a constant rate β_{CO}) from high to low values and back again. In Fig. 2(a) we plot the (negative) photocurrent measured in a PEEM experiment (which reflects the CO and oxygen coverage, respectively) as a function of CO partial pressure: note that a low photocurrent indicates an oxygen-covered, high current CO-covered Pt(111) surface. Figure 2(b) displays the (simultaneously measured) reactivity R_{CO_2} , i.e., the CO₂ production rate as detected mass spectrometrically, as a function of p_{CO} . On the left-hand side, i.e., for low p_{CO} , the Pt surface is essentially covered with oxygen (“oxygen side,” monostable region A), and the system is in the macroscopic stable steady state of high reactivity. In this steady state, the reaction rate (=CO₂ production rate) rises linearly with the CO pressure until, at $p_{CO} = \tau_A$ (flow rate F , p_{O_2} , T , β) the surface becomes covered with adsorbed CO. This “CO side” corresponds to the other macroscopic stable steady state of low reactivity, in which the low CO₂ production rate is caused by a more or less dense layer of adsorbed CO molecules which inhibits coadsorption of oxygen and, hence, the LH reaction to take place. After this transition, the system remains in the steady state of low reactivity located in the monostable region B. Even if the CO partial pressure is now reduced again, the system nevertheless remains in the less reactive state for a while. [The gradual decrease of the CO₂ signal of Fig. 2(b) is due to a decreasing background signal with the variation of p_{CO} and has no other physical origin]. As the CO partial pressure continues to fall, the system suddenly undergoes, at $p_{CO} = \tau_B(F, p_{O_2}, T, \beta)$, a steep

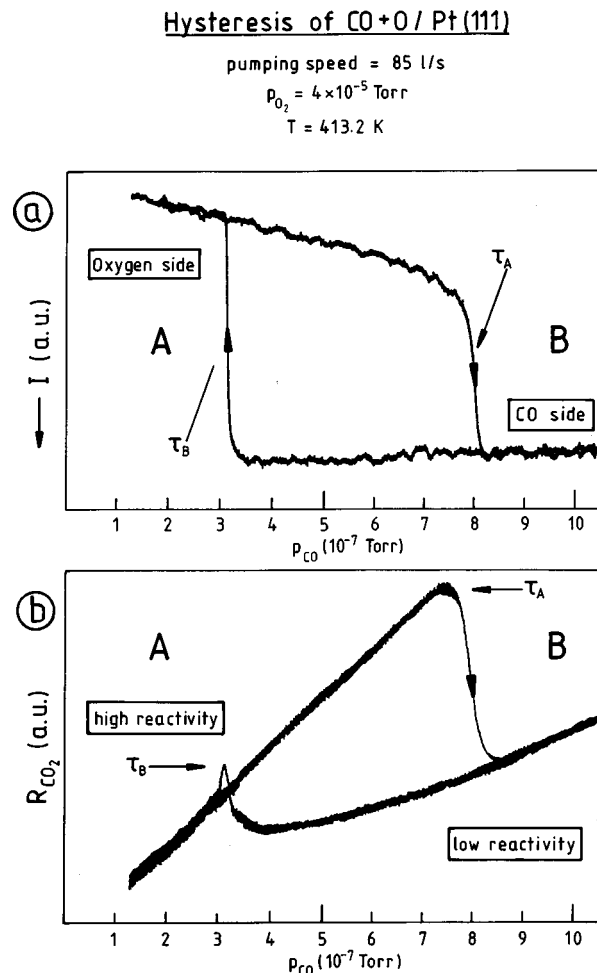


FIG. 2. Hysteresis in the reactant coverage [as measured by the PEEM photocurrent I , upper part, (a)] and in the CO₂ reaction rate [lower part, (b)]. The data were obtained with a Pt(111) surface upon cyclic variation of the CO partial pressure (plotted on the x axis) for otherwise constant external control parameters given in the head of the figures. The system is in the macroscopic steady state of high reactivity at low CO partial pressures, and in the macroscopic steady state of low reactivity at high CO partial pressures. A bistable region is located between the monostable regions A and B.

transition and rapidly returns to the initial steady state of high reactivity. In the following we denote τ_A and τ_B as (macroscopic) *transition points*, where the indices A and B denote the monostable region from which we departed in our experiments. Note that $\tau_A > \tau_B$.

From independent simultaneous measurements of the PEEM photocurrent a continuous change of the surface coverage is apparent also on the oxygen side, in a way that decreasing p_{CO} causes a decreasing CO coverage and increasing oxygen coverage, while in the steady state of low reactivity the CO coverage remains almost constantly high for a whole range of p_{CO} . This hysteresis allows us to subdivide the CO pressure regime into the two monostable regions A ($p_{CO} < \tau_B$) and B ($p_{CO} > \tau_A$), separated from each other by a bistable region ($\tau_A > p_{CO} > \tau_B$). In all *three* regions the system is either in one of the *two* macroscopic steady state of low or high reactivity.

Ehsasi *et al.*⁴⁷ showed that a variation of the CO pressure at constant oxygen partial pressure and at different sample temperatures T can elucidate the principal tempera-

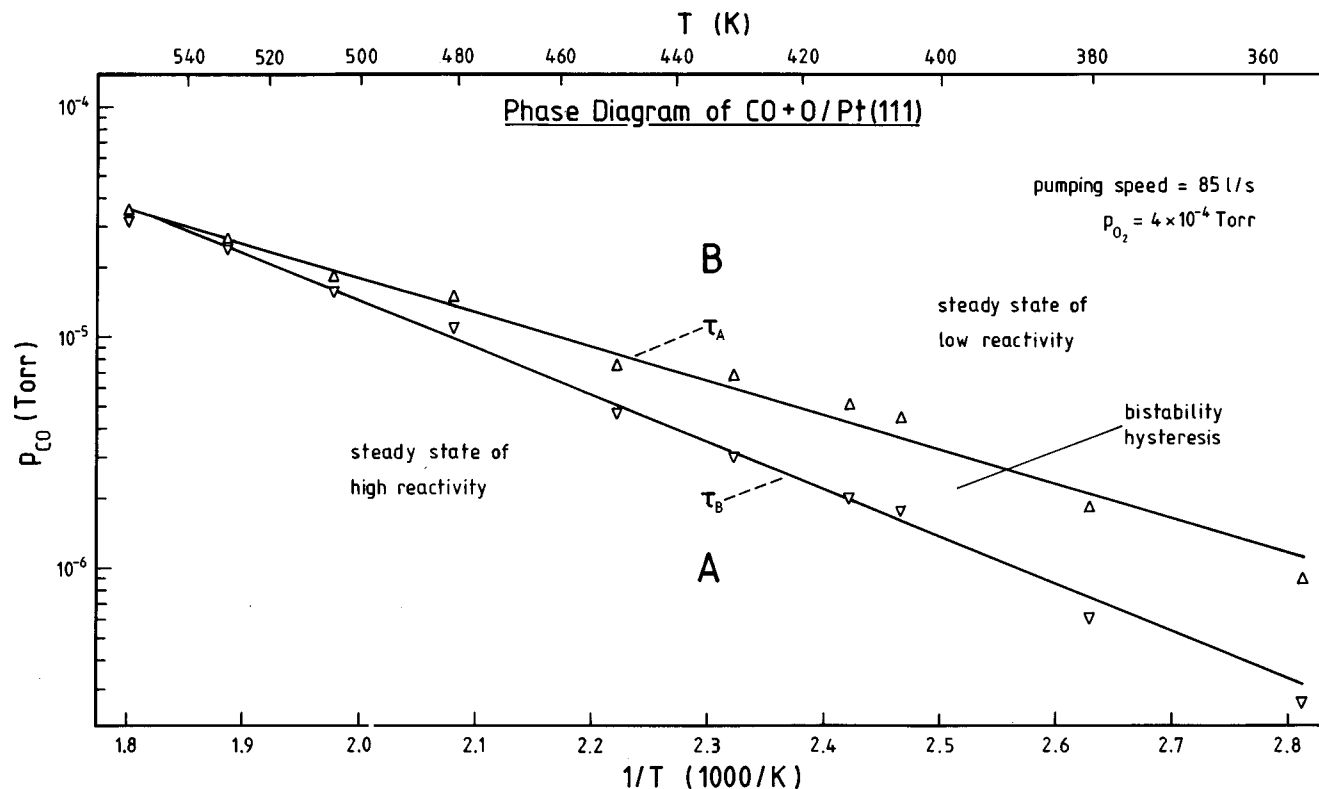


FIG. 3. Kinetic phase diagram of the CO oxidation on Pt(111): Plotted are the CO partial pressures of the macroscopic transition points τ_A and τ_B [cf. Fig. 2(b)] against the inverse temperature. The obtained "phase boundaries" separate the bistable region from the two monostable regions A and B over a large temperature interval. For convenience, an additional temperature scale is given on the upper ordinate. It is clearly demonstrated that the bistable region becomes narrower with increasing temperature and no longer exists beyond $T=550$ K.

ture influence on the reactive behavior of the system. (In this work the CO pressure was varied in one direction only. Due to this experimental restriction Ehsasi *et al.* did not detect a hysteresis for the CO oxidation on Pt(111) which was reported by Zhdanov and Kasemo²⁴). It is convenient to perform similar experiments as shown in Fig. 1, from which a plot of the CO partial pressure against the inverse temperature can be constructed. In this plot, the CO partial pressure values right at the macroscopic transition points τ_A and τ_B can be indicated and interconnected [cf., Fig. 2(b)]. The resulting p_{CO} vs $1/T$ representation then illustrates the phase boundaries separating the bistable region from the two monostable regions A and B over a large temperature range. Actually, it may be considered as a kind of a kinetic phase diagram (for a more elaborate explanation of this term, see Refs. 18 and 31). For Pt(111), the respective plot is shown in Fig. 3; for convenience, an additional temperature scale is given on the upper ordinate. Figure 3 clearly demonstrates that the bistable region becomes narrower with increasing temperature and no longer exists beyond $T=550$ K. In other words, no hysteresis in the CO oxidation appears for sample temperatures $T > 550$ K.

An entirely equivalent representation of the kinetic phase diagram which is shown as Fig. 4 consists of an *isothermal* plot of the CO partial pressure against the oxygen partial pressure (in Fig. 4, a constant sample temperature of 413.2 K was chosen). Again, the macroscopic transition points τ_A and τ_B are indicated and interconnected by a line. A short comment is necessary as regards the "construction"

of such a plot, because the data cannot be obtained by a single method over the whole range of parameter variation: For oxygen pressures *above* 10^{-5} Torr the reaction rate can easily be measured mass spectrometrically for any CO partial pressure; a single cycle is completed in about 30 min. The respective data points are indicated in Fig. 4 by open triangles. However, for oxygen pressures *below* 10^{-5} Torr, the transition between the two steady states is preferably monitored by the PEEM photocurrent (note that a CO and oxygen-covered surface can easily be distinguished here) rather than by mass spectrometry: At these low oxygen pressures and in view of the poor reactivity of the Pt(111) surface, the high flow rate of 85/s and the large reactor volume, the CO_2 production rate is swamped by the CO_2 background mass spectrometer signal. The detailed experimental procedure was as follows: When departing from monostable state B the oxygen pressure was steplike increased until the transition occurred. A 5 min interval was provided between the respective pressure changes to allow the transition to take place. We have marked the respective data points in Fig. 4 by full triangles.

Altogether, the isothermal phase diagram of Fig. 4 exhibits an interesting overall shape [compared to similar phase diagrams determined for the CO oxidation over Pt(210)¹² or Pd(110)¹⁸ where a crossing of the phase boundary lines was observed]: Within our data statistics, we rather obtain two *parallel* phase separation lines, which means that the width of the hysteresis does not depend on the CO and oxygen

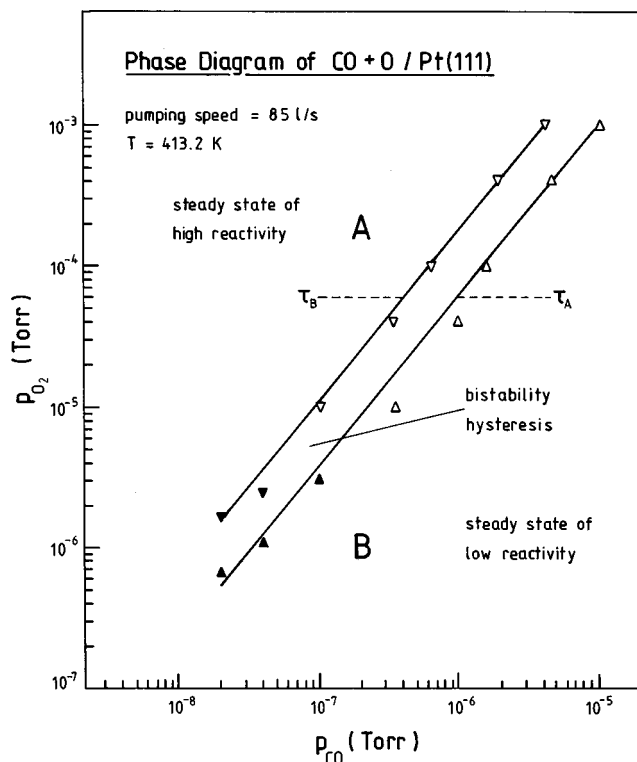


FIG. 4. The isothermal kinetic phase diagram ($T=413.2$ K) consists of a plot of the CO partial pressure against the oxygen partial pressure. Again, the macroscopic transition points τ_A and τ_B are indicated and interconnected by a line. These lines remain parallel at least within three decades of the CO and oxygen pressure spanned in our experiment. The different symbols of the data points reflect different modes of the measurement (see the text for details). Obviously, the monostable regions A and B are separated from each other by a region of bistability.

partial pressures, at least not for the set and range of external control parameters used in our experiments.

2. Time dependencies

For the following considerations the dynamical response of the system to intentional changes of the experimental control parameter(s) is of great interest. In the introductory chapter, we pointed already to the conclusion of Zhdanov and Kasemo,²⁴ who stated that the two branches of the hysteresis should fall together to the equistability point η , provided there occurs sufficiently rapid nucleation and growth of islands. We have, therefore, varied the scan rate of the CO partial pressure, $\beta_{CO}=dp_{CO}/dt$ from $\sim 4 \times 10^{-8}$ Torr/s to $\sim 6 \times 10^{-10}$ Torr/s (time t for a single scan between 4 min and 4 h). As illustrated in Fig. 5 by means of four examples ($t=5, 10, 60,$ and 120 min in one scan direction), we can clearly diagnose that the macroscopic transition points τ_A and τ_B approach each other and the width of the hysteresis shrinks with decreasing β_{CO} . The respective results are summarized in Fig. 6, which shows this narrowing effect even more clearly. However, due to experimental limitations we cannot establish scan rates lower than 10^{-10} Torr/s and are unable to decide whether or not the two branches will meet at still lower scan rates. Although our results could perhaps indicate a finite loop width of the macroscopically observed hysteresis also for infinitely slow scan rates this cannot positively be affirmed by the experimental procedure used here. In order to solve the principal problem of whether the hysteresis disappears for infinitely slow scan rate (as is stated by Zhdanov and Kasemo²⁴ for the condition of rapid creation

Time Dependence of the Hysteresis of CO+O/Pt(111)

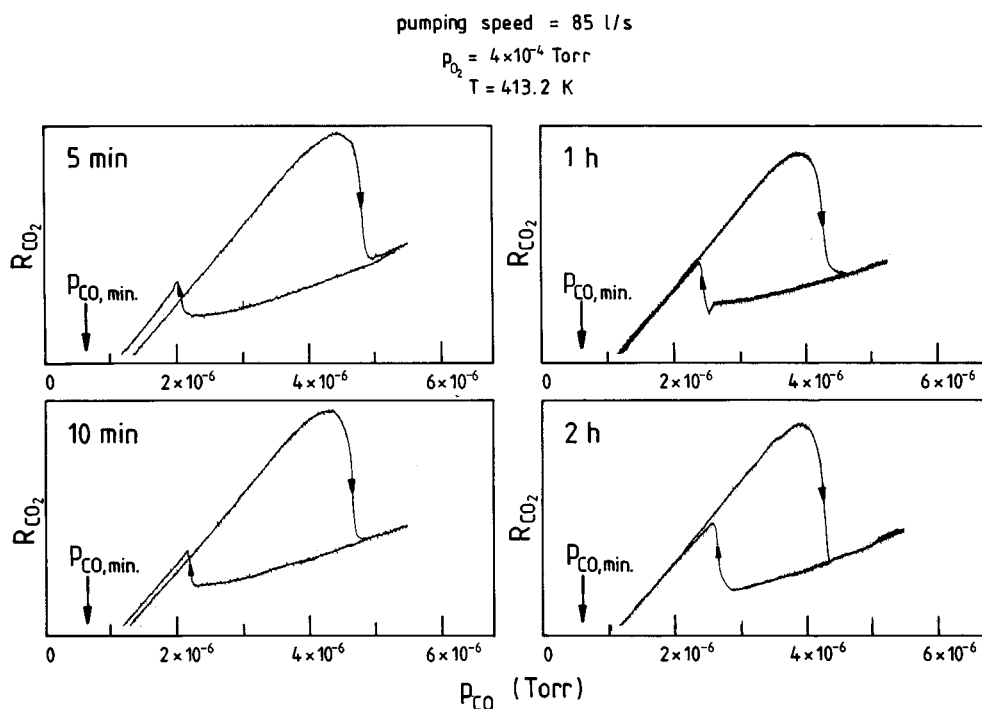


FIG. 5. Time dependence of the hysteresis of the reaction ($=CO_2$ production) rate on the scan rate of the CO partial pressure. The four examples of CO partial pressure variation shown refer to the scan times in each direction of 5, 10, 60, and 120 min, respectively. Apparently the macroscopic transition points τ_A and τ_B approach each other and the width of the hysteresis loop shrinks as the scan rate decreases.

Time Dependence of the Hysteresis of CO+O/Pt(111)

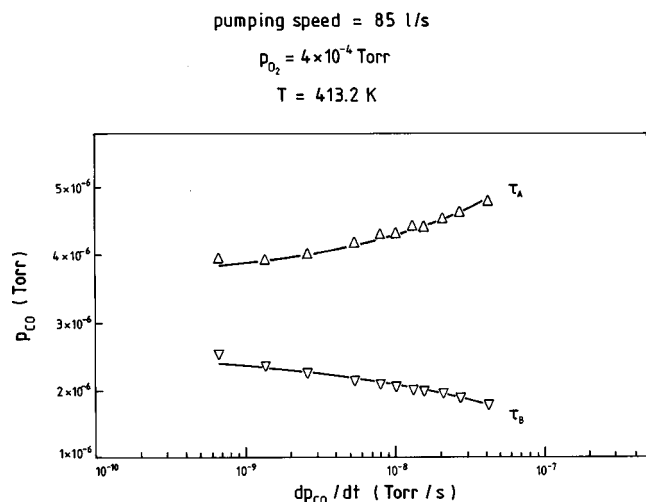


FIG. 6. Dependence of the macroscopic transition points τ_A and τ_B (and, hence, of the width of the hysteresis) on the scan rate of the CO pressure, $\beta_{CO} = dp_{CO}/dt$. Note that the width of the hysteresis shrinks as the scan rate is reduced to the lowest experimentally applicable scan rate of 6×10^{-10} Torr/s. Extrapolation to $\beta_{CO} \rightarrow 0$ seems to indicate a finite width of the hysteresis.

and propagation of the underlying chemical waves), one can invoke theoretical considerations and/or investigate the underlying phenomena no longer on a macroscopic, but on a mesoscopic (or microscopic) scale. In Sec. III B, we will show how useful the PEEM method is to tackle this problem, for it allows a very detailed study of the mesoscopic surface dynamical processes.

B. Spatiotemporal behavior on a mesoscopic scale

1. Pattern formation during cyclic scans of the CO partial pressure

The experiments described in Sec. III A allowed us to determine the macroscopic phase boundaries in the kinetic phase diagram, cf. Figs. 3 and 4. We can, therefore, preadjust certain combinations of external control parameters (preferably p_{CO} or p_{O_2} at constant T and F) and watch the mesoscopic morphology, in particular a spontaneous or assisted nucleation of CO or oxygen, in the photoelectron emission microscope. Another observation concerns the *role of crystallographic defects*. In both series of PEEM images one can clearly recognize mesoscopic surface inhomogeneities, which most likely represent crystallographic defects (point or screw dislocations, steps, pin holes, etc.). Unfortunately, their internal morphology cannot be determined, due to the limited resolution of PEEM. We realize, however, that a few defects are very active with respect to the nucleation of CO and oxygen, while others are not. These “active” inhomogeneities act as nucleation centers either for the formation of CO islands (*CO-type defects*) or oxygen islands (*oxygen-type defects*).

In Fig. 7 we present two plots of the reaction (i.e., CO_2 formation) rate versus the CO pressure, for fixed oxygen partial pressure $p_{O_2} = 4 \times 10^{-4}$ Torr and temperature ($T = 413.2$ K). Two hystereses are observed which can be di-

Hysteresis of CO+O / Pt(111)

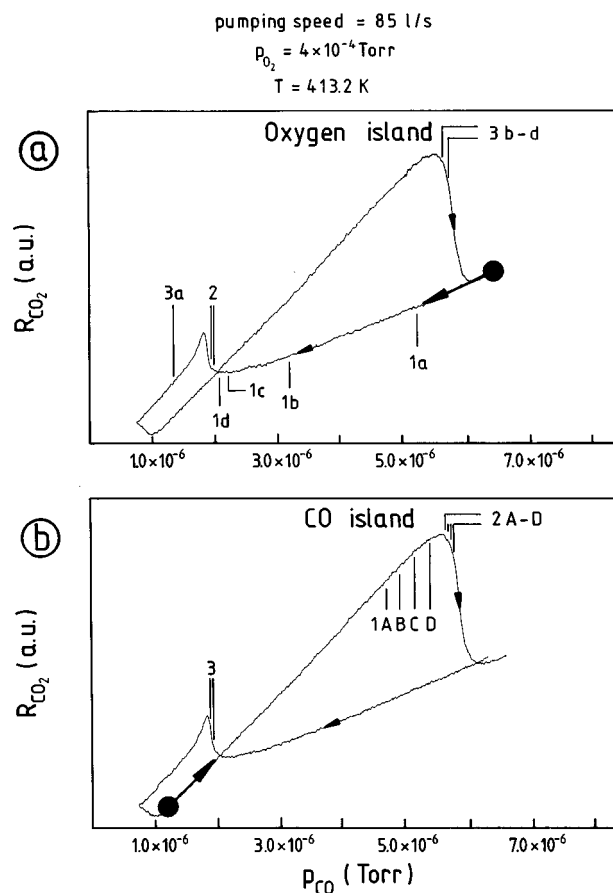


FIG. 7. Two plots of the reaction rate vs CO partial pressure. The hysteresis displayed in the top (a) concerns a surface region in which an oxygen-type defect is located. The hysteresis shown in the bottom (b) refers to CO-type defects which promote the formation of *carbon monoxide* islands. The two hystereses are directly correlated with the (simultaneously measured) series of PEEM images presented in Figs. 8 and 9. The marks on the curves indicate the momentary CO partial pressure at which the PEEM images presented in these two figures were taken. The dark dots mark the beginning of the series in Figs. 8 and 9 (time $t=0$).

rectly correlated with the (simultaneously measured) series of PEEM images presented in Figs. 8 and 9. The *upper* hysteresis [Fig. 7(a)] concerns a surface region in which an oxygen-type defect is located. This gives rise to the formation or disappearance of *oxygen* islands (we recall that they appear *dark* on a gray background), while the *lower* hysteresis [Fig. 7(b)] is linked to three CO-type defects which promote the formation of *carbon monoxide* islands (they appear *bright* on a gray PEEM background). We also emphasize that the two series of PEEM images (diameter $380 \mu\text{m}$) concern surface patches which are only $\sim 500 \mu\text{m}$ far apart; consequently, local pressure gradients due to shielding effects (possibly caused by the PEEM entrance lens) are practically identical for both surface areas.

We will now describe the typical spatiotemporal behavior in the environment of an oxygen-type defect and the resulting growth of oxygen islands during a CO pressure scan. For this purpose, we present, in Fig. 8, a series of PEEM images and keep Fig. 7(a) in mind. We start off with a completely CO-covered Pt(111) surface in the monostable region

PEEM images of CO+O / Pt(111)

F (l/s)	p_{CO} (Torr)	p_{O_2} (Torr)	T (K)	Δt (s)
85	∇	4×10^{-4}	413.2	-

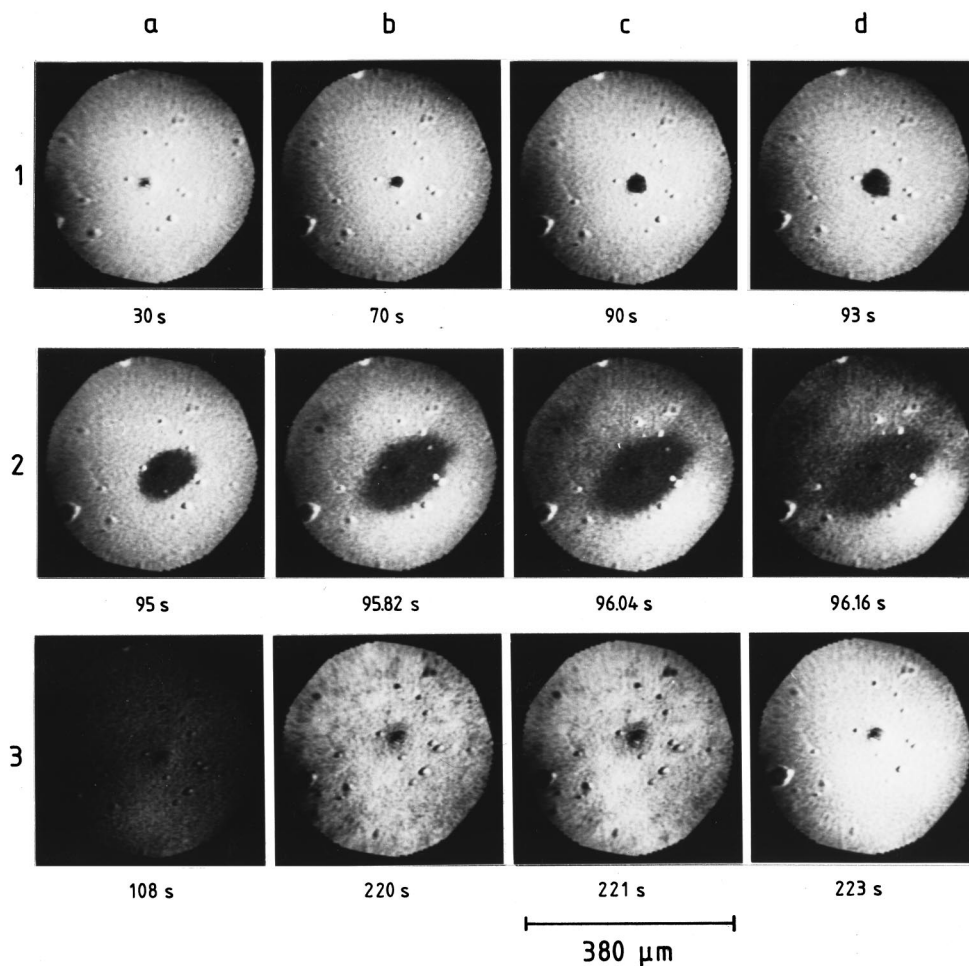
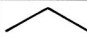


FIG. 8. Series of PEEM images taken in a surface region with one oxygen-type defect. Each image displays a circular area of $380 \mu\text{m}$ in diameter. The head of the figure contains the relevant external control parameters and also shows how the CO pressure scan was performed (first $\beta_{\text{CO}} < 0$, then $\beta_{\text{CO}} > 0$). Note that the oxygen island appears dark on a bright background; during the first half-cycle, the oxygen island nucleates at the oxygen-type defect [Fig. 8(1)], followed by a spontaneous nucleation of oxygen in the vicinity of the oxygen island [Fig. 8(2)]. Spontaneous nucleation of CO, on the other hand, occurs during the second half-cycle [Fig. 8(3)]. The CO pressure scan belonging to this series of images is monitored in Fig. 7(a).

B and proceed from the dark dot indicated in Fig. 7(a) along the arrow (the CO partial pressure is slowly lowered). In addition, the respective PEEM “snapshots” taken along this course are marked whereby we use the same notation as in Fig. 8. Turning to Fig. 8, we present a series of such snapshots while the CO partial pressure is gradually reduced [Figs. 8(1) and 8(2)] and increased again [Fig. 8(3)]. One clearly observes a small (dark) oxygen island formed at a defect approximately in the middle of the PEEM image and still surrounded by a dense CO environment, cf. Figs. 8(1a) and 8(1b), long before the transition to the steady state of high reactivity occurs. Approximately 20 s later [Fig. 8(1c)]—during these 20 s the oxygen nucleus expands only slightly—the radius of the oxygen island increases quite rapidly within a period of only ~ 6 s, cf. Figs. 8(1c) to 8(2d),

and the surrounding area of the island becomes spontaneously covered with oxygen. Finally, the system is in the steady state of high reactivity as monitored by Fig. 8(3a). Here, most of the CO molecules have been reacted off and replaced by oxygen, and there appears no PEEM contrast anymore. The macroscopic reaction rate follows the same trend as can be deduced again from Fig. 7(a), upper half. Note that this rate was measured in a completely parallel fashion. Figures 7 and 8 both prove that the formerly inactive system transforms to a reactive one as CO molecules are increasingly replaced by oxygen atoms. We are well aware that there is an apparent difference in the reaction rate R_{CO_2} between decreasing and increasing CO partial pressures in the high-reactivity range of Fig. 7: for $p_{\text{CO}} = 2 \times 10^{-6}$ Torr

PEEM images of CO+O / Pt(111)

F (l/s)	p_{CO} (Torr)	p_{O_2} (Torr)	T (K)	Δt (s)
85		4×10^{-6}	413.2	0.24–5.0

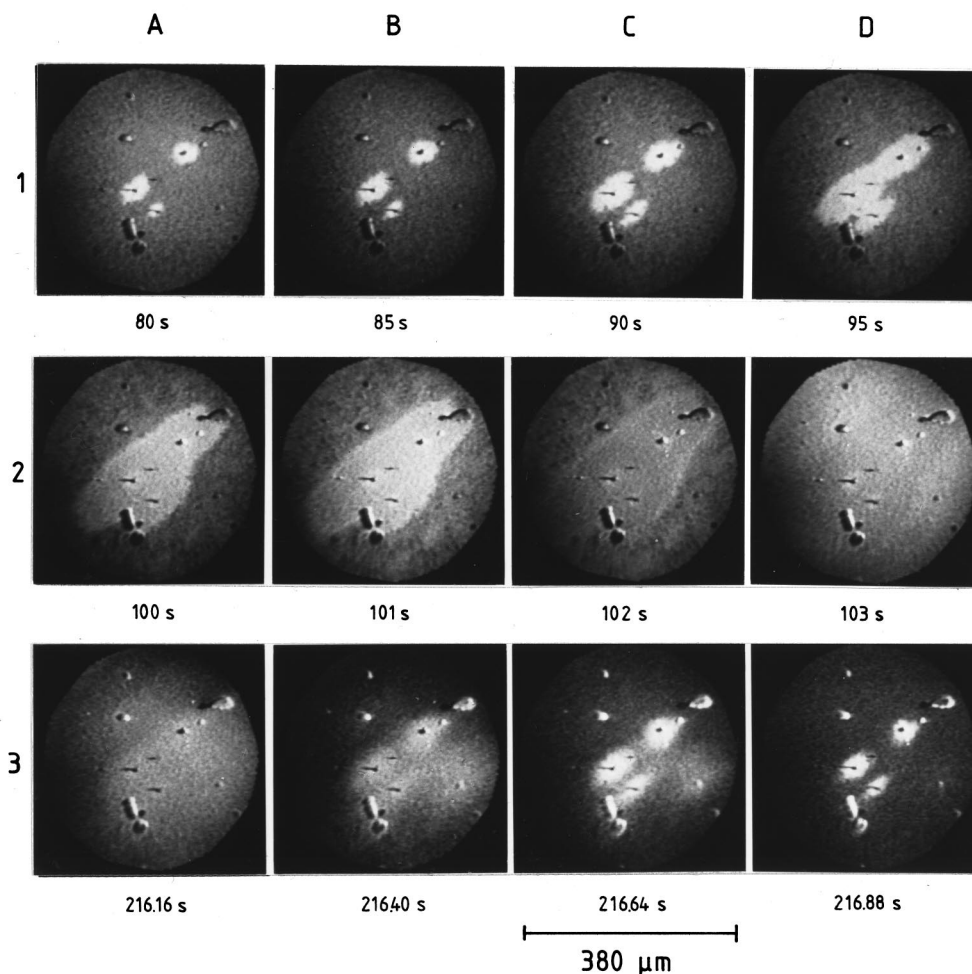


FIG. 9. Series of PEEM images taken in a surface region with three CO-type defects. Again, each image displays a circular area of $380 \mu\text{m}$ in diameter, the external control parameters and the principle course of the p_{CO} scan can be taken from the head of the figure. The parallel reactivity of the Pt(111) surface can be judged from Fig. 7(b). For $\beta_{\text{CO}} > 0$ the assisted nucleation of CO islands [Fig. 9(1)] competes with the spontaneous nucleation that occurs in the vicinity of the CO islands [Fig. 9(2)], while for $\beta_{\text{CO}} < 0$ only spontaneous nucleation of oxygen can be observed [Fig. 9(3)].

the rate for negative p_{CO} scan surmounts the one observed during positive p_{CO} scan. This experimental artifact is caused by the rapid variation of the CO pressure and the concomitant phase lag between the electronic pressure regulation and the actual chamber pressure; however, it does not affect the position of the reactivity maxima on the p_{CO} scale. For increasing CO pressure, the reaction-rate maximum appears at 5.5×10^{-6} Torr, for decreasing p_{CO} the reactivity is highest at 1.7×10^{-6} Torr.

The PEEM images presented in Fig. 8(3) monitor the behavior for increasing p_{CO} and the transition back to the macroscopic steady state of low reactivity. They demonstrate that CO islands are not formed at these defects, and the overall CO coverage is mainly the result of spontaneous nucleation which takes place everywhere on the Pt(111) surface.

Nevertheless, local oxygen coverages may survive for a rather long time right at those oxygen-type defects or surface inhomogeneities from which the oxygen islands initially originated.

Next we turn to the counterpart, namely to the behavior in the vicinity of three CO-type defects and discuss the nucleation, growth, and off-reaction of CO *islands* during a CO pressure cycle. The overall situation is illustrated by means of Fig. 9. As before with oxygen, the parallel reactivity of the Pt(111) surface can be judged from Fig. 7(b), in which we mark the point of departure by a dark dot and the direction of our cycle by an arrow. Note that both cycles in Fig. 7 were performed one after the other. Again, the PEEM snapshots presented in Figs. 9(1A)–9(1C), etc. are indicated. Initially, the surface is completely covered with oxygen. Fig-

ures 9(1A)–9(1D) then show the beginning nucleation and growth of CO islands in an oxygen environment, whereby the nucleation of CO, too, takes place preferentially at the three aforementioned defect sites. The CO islands grow rapidly and coalesce [Fig. 9(1)]. The respective large island continues to grow [Fig. 9(2A)], until a spontaneous nucleation of CO reacts off all the surrounding oxygen, a situation that is monitored in Figs. 9(2C) and 9(2D). Figure 9(2D) then represents a completely CO-covered, inactive Pt(111) surface. The subsequent lowering of the CO pressure (negative scan) leads to the sequence of PEEM images shown in Figs. 9(3A)–9(3D): While large oxygen islands are not formed in this local area of the surface, we find a very fast ($t < 1$ s) spontaneous nucleation of oxygen [Figs. 9(3B)–9(3D)]. Just the direct vicinity of the three CO-type defects can keep its local CO coverage for a longer time period [Fig. 9(3D)]; a behavior similar to what occurred near the oxygen-type defect. We recall our remarks made in Sec. I and refer especially to the description of a cycle given in Fig. 1. The situation we just described is representative for a fast scan experiment characterized in Fig. 1(c) by the sequence of PEEM patterns $\{1\} \rightarrow (2b) \rightarrow \{3\} \rightarrow (4b) \rightarrow \{1\}$.

2. Pattern formation after steplike changes of the CO partial pressure

a. Positive or negative steplike changes of CO partial pressure. We were particularly interested in how the transitions between the two macroscopic stable steady states are reflected in the spontaneous nucleation and especially in the island growth and performed systematic PEEM experiments. We followed the relaxation of the reactive system after the CO partial pressure had been steplike decreased (increased) and kept on a constant level. To better understand the various ‘‘jump’’ experiments we recall the diagram of Fig. 1(c) in which these ‘‘jumps’’ are indicated by arrows. The PEEM observations are summarized in Fig. 10 for the oxygen and in Fig. 11 for the carbon monoxide nucleation. Figures 10(a) and 11(a) refer to the *slow assisted* nucleation and growth of large islands [Fig. 1(c) states (2) and (4a)] while Figs. 10(b) and 11(b) refer mainly to the *rapid spontaneous* nucleation of small patches [Fig. 1(c) states (2b) and (4b)].

All relaxation experiments were carried out at a constant flow rate of 85/s, a constant oxygen partial pressure of 4×10^{-4} Torr, and a constant sample temperature of 413.2 K. In order to study the nucleation and growth of oxygen islands in a dense CO adlayer we first generated a fully CO-covered Pt(111) surface by adjusting a stationary CO pressure of 5.9×10^{-6} Torr. This combination of external control parameters drives the system safely into the *stable* steady state of low reactivity [state $\{3\}$ in Fig. 1(c)]. The time required for this state to form is less than 60 s. After these 60 s, the CO pressure was suddenly (i.e., within $\Delta t_{\text{jump}} \approx 10$ s) lowered to a new steady value. In a typical experiment [which is the basis of the PEEM patterns of Fig. 10(a)] a relatively moderate CO pressure jump of $\Delta p_{\text{CO}} = -3.19 \times 10^{-6}$ Torr to the final value $p_{\text{CO}} = 2.71 \times 10^{-6}$ Torr was chosen [in Fig. 1(c): change of state $\{3\} \rightarrow (4a) \rightarrow \{1\}$]. In contrast, we adjusted the larger pressure drop of $\Delta p_{\text{CO}} = -4.42 \times 10^{-6}$ Torr to a final value of $p_{\text{CO}} = 1.48 \times 10^{-6}$ Torr in Fig. 10(b) [change of

state, according to Fig. 1(c) $\{3\} \rightarrow (4b) \rightarrow \{1\}$]. The moment of the CO pressure jump is defined as $t = 0$ s.

According to Fig. 1(c), we depart in the first experiment with its lower Δp_{CO} from state $\{3\}$ and follow the arrow to the left. The system becomes metastable (dash-dotted line), we pass the transient state (4a) and end up with the stable steady state $\{1\}$ right inside the region of assisted nucleation, but outside the region of experimental bistability [Fig. 1(c): $\mu_{\text{B}} < p_{\text{CO}} < \nu_{\text{B}}$]. The associated mesoscopic surface structure is documented by Fig. 10(a) which provides a sequence of 12 PEEM images taken after continuous time intervals Δt (given in the legend of the Fig. 1). Two effects deserve attention. First, there occurs a remarkable induction period: it is not until 780 s that a (dark) oxygen nucleus right in the middle of the image begins to expand [Fig. 10(a,1a)]. Second, a comparatively slow growth process takes place after this induction period which we illustrate by the sequence of PEEM images taken after subsequent time intervals Δt of 10 s [20 s between images 2(d) and 3(a)]. Note that the sample has been moved to the left after the images 2(b), 2(c), 2(d) and down after 3(b) were taken. In the final image, cf. Fig. 10(a3d) only a small surface area is left covered with CO, by far the majority of the Pt(111) surface has become covered with adsorbed oxygen. We emphasize that, for this choice of external control parameters, we never succeeded in obtaining spontaneous nucleation in a manner described above for our CO pressure-scan experiments.

We comment now on the second kind of jump experiment with its larger CO pressure drop [cf. Fig. 10(b)] and refer again to the general scheme of Fig. 1(c). As before, we start off from state $\{3\}$ and rapidly reach state (4b); thereafter, the system moves into steady state of high reactivity $\{1\}$ which is located right inside the monostable region A [Fig. 1(c): $p_{\text{CO}} < \mu_{\text{B}}$]. First, there occurs nucleation and growth of an individual oxygen island as documented by the single (dark) spot in the center of the PEEM image. Already 17 s after the CO pressure jump this oxygen island is clearly visible and grows rapidly during the forthcoming 3 s [Fig. 10(b,1)]. While this island apparently nucleates at a surface defect (and may thus indicate assisted nucleation) evidence also of spontaneous nucleation is provided by the sudden rise of the ‘‘dark’’ PEEM background ~ 20 s after the CO pressure has been dropped [cf. Fig. 10(b2)]. This behavior is indicative of a more homogeneously increasing oxygen coverage also in the formerly CO-covered region. A very short time interval ($t < 1$ s) is then sufficient to complete the transition to the entirely oxygen-covered surface [as indicated by the disappearance of the black/white contrast and its replacement by a rather diffuse granulated gray background, c.f. Fig. 10(b,3d)]. In its final state, the system has transformed to the stable steady state of high reactivity, as pointed out above.

A completely analogous procedure was now used to follow the nucleation of *carbon monoxide* in an oxygen environment, i.e., on the oxygen covered Pt(111) surface. Again, we first generated a well-defined initial state of the Pt(111) surface by adjusting an appropriate (fairly large) oxygen partial pressure ($p_{\text{O}_2} = 4 \times 10^{-4}$ Torr) at $T = 413.2$ K, while the CO pressure was held at the comparatively low value of

PEEM images of CO+O / Pt(111)

F (l/s)	p_{CO} (Torr)	p_{O_2} (Torr)	T (K)	Δt (s)
85	2.71×10^{-6}	4×10^{-4}	413.2	10

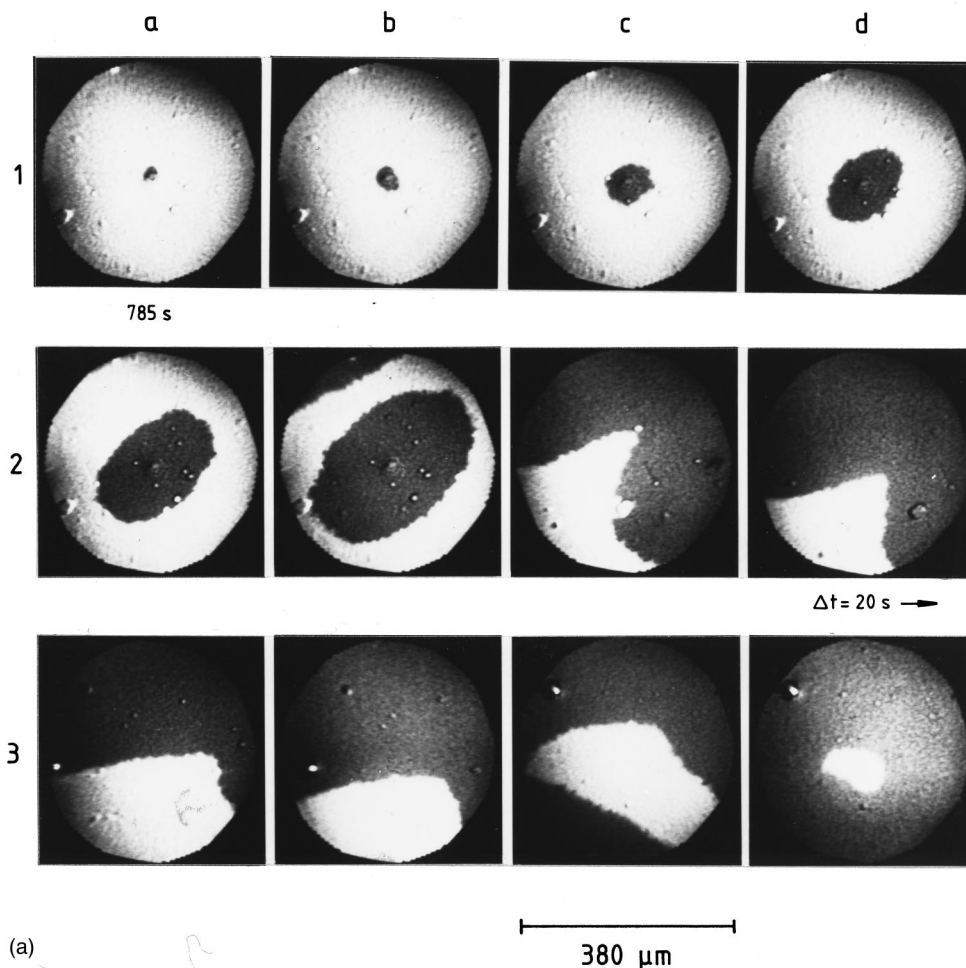


FIG. 10. (a) Time dependence of the oxygen island growth after the CO partial pressure was steplike lowered ($\Delta p_{\text{CO}} = -3.2 \times 10^{-6}$ Torr). In Fig. 1(c) the change of the reactant surface morphology corresponds to the route $\{3\} \rightarrow (4a) \rightarrow \{1\}$. The transition to the final steady state of high reactivity takes place via an assisted nucleation of oxygen. The time intervals Δt between the individual images were 10 s [20 s between image (2d) and (3a)], beginning only 785 s after the jump. The other external control parameters are given in the head of the figure. (b) Series of PEEM images similar to Fig. (b), but for a larger steplike decrease of the CO partial pressure of $\Delta p_{\text{CO}} = -4.4 \times 10^{-6}$ Torr. According to Fig. 1(c), a change of lateral state was performed along the route $\{3\} \rightarrow (4b) \rightarrow \{1\}$. Here, the transition to the steady state of high reactivity proceeds via a spontaneous nucleation of oxygen. The intervals between the PEEM snapshots are indicated.

1.5×10^{-6} Torr. As before, these external control parameters ensured that the system rapidly reached and stayed in the stable steady state of high reactivity (oxygen-covered surface, monostable region A). After stabilization of this phase, ‘‘jump’’ experiments were performed with the CO partial pressure being steplike raised to increasingly larger stationary values. According to Fig. 1(c), we depart from state $\{1\}$ and move from left to right: The small $\Delta p_{\text{CO}} = +3.1 \times 10^{-6}$ Torr to the constant CO pressure of 4.6×10^{-6} Torr [Fig. 1(c): $\nu_A < p_{\text{CO}} < \mu_A$] thereby drives the system [via the transient state (2a)] far into the region of assisted nucleation (but still outside the region of experimental bistability). The rather larger pressure jump of $\Delta p_{\text{CO}} = +4.4 \times 10^{-6}$ Torr to

$p_{\text{CO}} = 5.5 \times 10^{-6}$ Torr [Fig. 1(c): $\mu_A < p_{\text{CO}}$], however, drives the system, via the transient state (2b), far into the monostable region B (steady state $\{3\}$). As before, we have monitored the respective changes in the PEEM patterns and reproduce these in Figs. 11(a) and 11(b), respectively.

The series of six PEEM images shown in Fig. 11(a) represents a change of state along the route $\{1\} \rightarrow (2a) \rightarrow \{3\}$ of Fig. 1(c). This series illustrates that the small positive CO pressure jump causes a slow growth of three (bright) CO islands in the (dark) environment of the oxygen-covered surface [Fig. 11(a1)], whereby the islands nucleate at defects. The first nuclei begin to expand after the considerable induc-

PEEM images of CO+O / Pt(111)

F (l/s)	p_{CO} (Torr)	p_{O_2} (Torr)	T (K)	Δt (s)
85	148×10^{-6}	4×10^{-4}	413.2	0.08 - 1.0

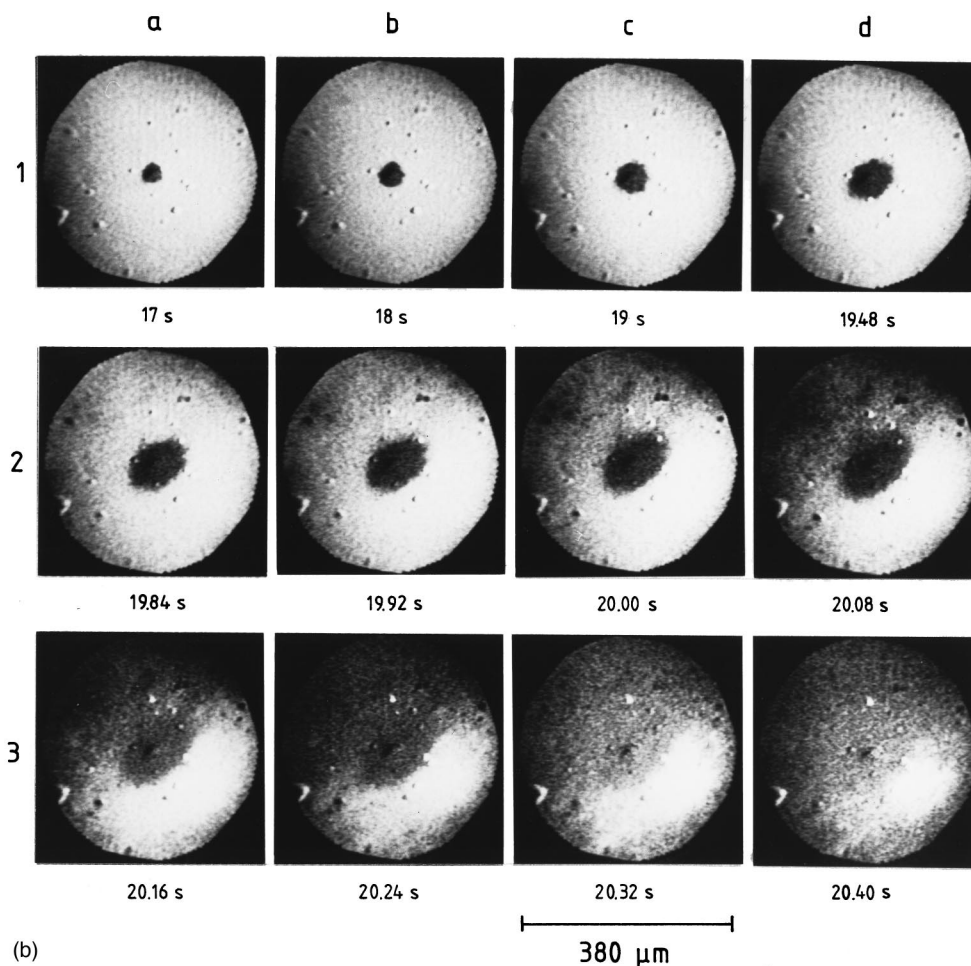


FIG. 10. (Continued.)

tion time of 47 s, and within the next ~ 90 s the three CO patches merge into a single large island.

The eight PEEM images of Fig. 11(b) (taken at time intervals Δt of 2 s) reflect the situation of a larger positive jump of the CO pressure [change of state along the route $\{1\} \rightarrow \{2b\} \rightarrow \{3\}$ of Fig. 1(c)]. Again, three CO islands nucleate at the three defects; they expand 5.5 s after the pressure rise. Compared to the other experiment, this induction time is by a factor of 10 shorter. Within the next 6 s the islands grow considerably and coalesce to a single large island [Fig. 11(b1)]. Analogous to the defect-mediated assisted nucleation of oxygen islands, a spontaneous nucleation and growth of CO islands is suggested by Fig. 11(b2), in which somewhat more extended white patches (reflecting CO nuclei) appear inside the dark “sea” of the oxygen adsorbate layer.

A final note concerns the observation whereafter both CO and oxygen islands sometimes exhibit an elliptical shape,

while one would expect, for the isotropic (111) surface orientation, rather circular islands. However, recent LEEM experiments (low energy electron microscopy)^{32,33} reveal that anisotropic steps and kinks may be inhomogeneously distributed across the surface and can facilitate anisotropic island growth.

The four jump experiments described above were selected here as representative for a whole variety of quantitative PEEM measurements at different Δp_{CO} values, for otherwise constant external control parameters. They clearly localize the boundaries which separate the regions of spontaneous and assisted nucleation and allow us to map the “experimental” bistable region as part of the computed bistable region. In these jump experiments, we systematically varied the final partial pressure of CO and adjusted especially those values which drive the system to the region of assisted nucleation. We followed both the corresponding induction times t_{ind} and the radii of the respective islands of CO and oxygen,

PEEM images of CO+O / Pt(111)

F (l/s)	p_{CO} (Torr)	p_{O_2} (Torr)	T (K)	Δt (s)
85	4.59×10^{-6}	4×10^{-4}	413.2	30

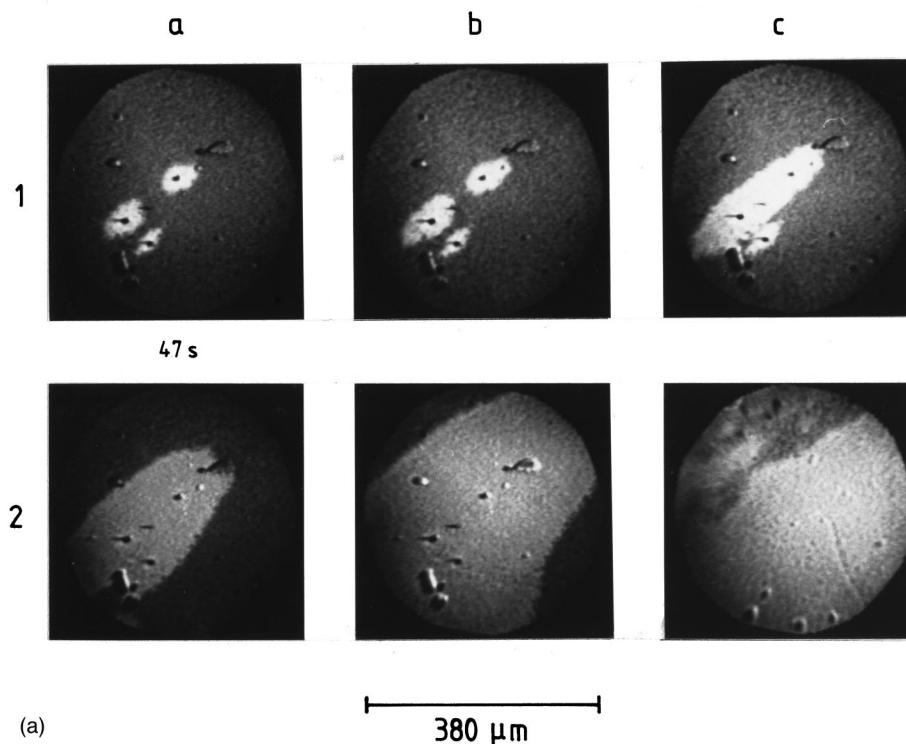


FIG. 11. (a) Time dependence of the nucleation and growth of carbon monoxide islands. The same procedure as in Fig. 10 was applied except that a positive CO pressure jump of $\Delta p_{\text{CO}} = +3.1 \times 10^{-6}$ Torr was performed along the route $\{1\} \rightarrow (2a) \rightarrow \{3\}$ of Fig. 1(c), i.e., an assisted nucleation transforms the system into stable steady state of low reactivity. (b) Eight PEEM images taken in the same mode as described for (a) except the fact that a larger positive CO pressure jump of $\Delta p_{\text{CO}} = +4.4 \times 10^{-6}$ Torr was applied. In Fig. 1(c), the system follows the route $\{1\} \rightarrow (2b) \rightarrow \{3\}$. Again, three CO islands nucleate at CO-type defects; they expand 5.5 s after the pressure rise, but spontaneous nucleation drives the system rapidly into the stable steady state of low reactivity. Compared to the experiment in (a), the induction time is by a factor of 10 shorter.

r_{CO} and r_{ox} as a function of the associated CO partial pressure, while all other external control parameter F , p_{O_2} , and T were kept constant. To determine the “radius” of islands with elliptic shape we measured the distance of the front with respect to the “active” stationary defect where the nucleation takes place in a given direction (shortest distance). Our results are summarized in Fig. 12. The top part shows the radius of the oxygen islands, the bottom part the radius of the carbon monoxide islands both as a function of time, for various final CO partial pressures p_{CO} which were steplike adjusted at time $t=0$ s. In order to make oxygen islands grow, negative pressure jumps Δp_{CO} were chosen (whose values follow from the relation $\Delta p_{\text{CO}} = p_{\text{CO}} - 5.9 \times 10^{-6}$ Torr). For the growth of carbon monoxide islands, Δp_{CO} was adjusted positive, according to the relation $\Delta p_{\text{CO}} = p_{\text{CO}} - 1.5 \times 10^{-6}$ Torr). The (constant) pressures p_{CO} were chosen such that the system ended up somewhere in or between the region of spontaneous and assisted nucleation, respectively, in a manner indicated in Fig. 1(c). We empha-

size that the examples that led to Figs. 10 and 11 are a part of these systematic measurements.

All growth curves show a common behavior in that an initial range of small or vanishingly small growth velocity (which may well be considered as an induction period) is clearly separated from a steeply increasing and finally constant growth rate. Although the physical behavior of the system depends on where in the $\$$ -shaped diagram it is driven by the actual jump of the external control parameter p_{CO} [see Fig. 1(c)], we can illustrate the general behavior in a simpler fashion by the difference (jump “height”) of the initial and final CO pressure, Δp_{CO} : Small heights Δp_{CO} cause a large induction time t_{ind} and slow front motion, while a large Δp_{CO} leads to short t_{ind} values and rapid growth. Furthermore, it is remarkable how sensitive just the induction time t_{ind} (during which the nuclei do not really grow) depends on p_{CO} , while the final growth rate is much less dependent on this quantity.

The essence of Fig. 12 is summarized in Fig. 13. This

PEEM images of CO + O / Pt(111)

F (l/s)	p_{CO} (Torr)	p_{O_2} (Torr)	T (K)	Δt (s)
85	5.54×10^{-6}	4×10^{-4}	413.2	2

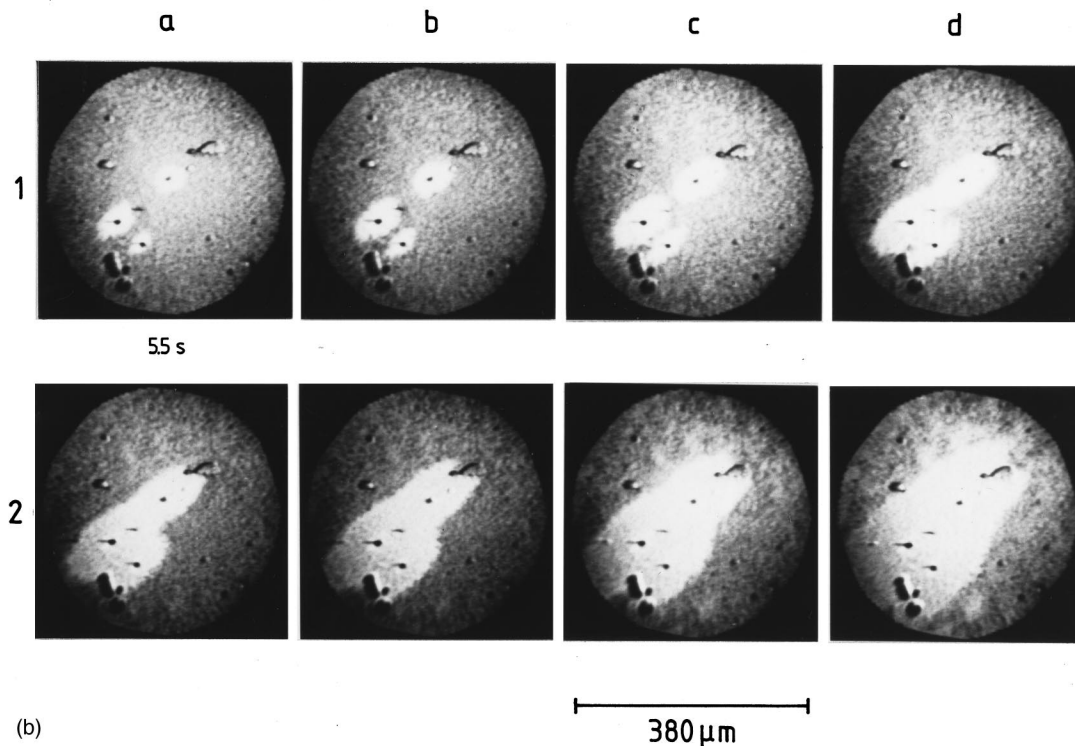


FIG. 11. (Continued.)

figure consists of two principal diagrams, namely, a plot of the aforementioned induction time t_{ind} against the CO partial pressure p_{CO} for both oxygen islands (small p_{CO} , left-hand side) and CO islands (large p_{CO} , right-hand side), Fig. 13(a), and the dependence of the growth rate (front velocity) on the CO partial pressure, Fig. 13(b). [The bottom graph 13(c) is merely a magnification of the diagram b and will be discussed further below]. The induction times t_{ind} for the island growth given in Fig. 13(a) were determined by linear extrapolation of the steep slope of the curves displayed in Fig. 12 to the hypothetical zero radius. Figure 13(b) exhibits two principally different ranges of island growth velocity: For small Δp_{CO} values, this velocity is rather small, but a larger Δp_{CO} accelerates this growth considerably. (For internal consistency, we have given the growth rate of the oxygen islands a *negative* sign, since an expansion of a CO-covered surface patch causes a parallel shrinking of the O-covered surface area). The reason behind this behavior is that the islands expand much faster if spontaneous nucleation is possible in the surface areas surrounding the islands. We have determined the border line between velocity regimes and are able to locate the points $\mu_{\text{A,B}}$ in Fig. 1(c) as follows: $\mu_{\text{B}} \approx 2.3 \times 10^{-6}$ Torr $< p_{\text{CO}} < 5.5 \times 10^{-6}$ Torr $\approx \mu_{\text{A}}$.

As Fig. 13(c) proves, there is a range of CO partial pres-

ures in which the velocity of island expansion varies practically linearly with the CO pressure. One can now extrapolate the linear sections of the growth velocity-vs- p_{CO} -relation toward zero velocity [dashed lines in Fig. 13(c)] and can immediately deduce that this graph seems to predict a peculiar range of CO pressures ($\nu_{\text{B}} \approx 3.1 \times 10^{-6}$ Torr $< p_{\text{CO}} < 3.5 \times 10^{-6}$ Torr $\approx \nu_{\text{A}}$) in which both CO and oxygen islands should exhibit *zero growth velocity*. We denote this particular interval as the region of experimental bistability. In the following section, we present additional experiments that characterize this region.

b. Positive and negative steplike changes of CO partial pressure. The investigation of the experimental bistable region if we start off from the monostable region A (B) and conduct two pressure changes: The first such change Δp_{CO} is positive (negative), and the second one is negative (positive). The first jump right into the range $\nu_{\text{A}} < p_{\text{CO}} < \mu_{\text{A}}$ ($\mu_{\text{B}} < p_{\text{CO}} < \nu_{\text{B}}$) causes supercritical nuclei of CO (oxygen) to form, and islands begin to grow. The second jump to the interval $\nu_{\text{B}} < p_{\text{CO}} < \nu_{\text{A}}$ follows, once the island has reached a considerable size of some 100 μm . In performing these two changes in p_{CO} we follow the route $\{1\} \rightarrow \{2\text{a}\} \rightarrow \{5\}$ and $\{3\} \rightarrow \{4\text{a}\} \rightarrow \{5\}$, respectively, in Fig. 1(c). After the first pressure jump the system behaves as described above, but

Island growth during CO oxidation / Pt(111)

pumping speed = 85 l/s

$p_{O_2} = 4 \times 10^{-4}$ Torr

$T = 413.2$ K

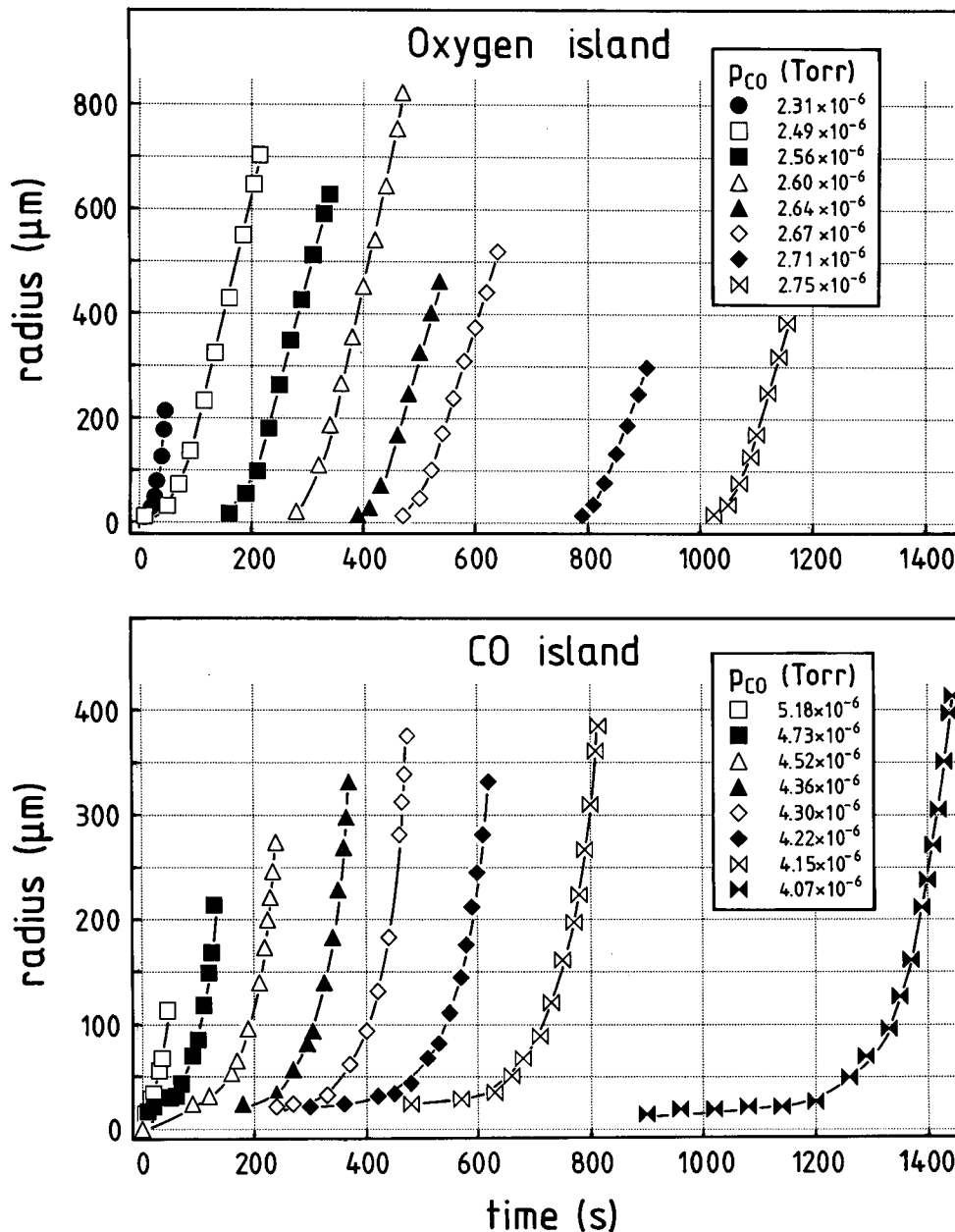


FIG. 12. Condensation of the results of the “pressure jump” experiments (Figs. 10 and 11): *Upper panel*: Growth rate of the oxygen island (as determined by the time dependent increase of the radius of the island) for various p_{CO} values (the final CO partial pressures are indicated in the inset). *Lower panel*: Respective growth rate of the carbon monoxide islands.

immediately after the second Δp_{CO} the front velocity slows down and finally comes to a complete standstill. Accordingly, one can observe islands or fronts that *do not or hardly move anymore*—in an especially lucky experiment we succeeded in keeping the front of an oxygen island immobile for 12 hours! The immobility could be quite clearly concluded from difference images where the initial PEEM patterns of

the fronts were subtracted from the ones obtained after a certain time interval. Except for some small fluctuations due to the mechanical vibrations of the sample holder there were no indications of any change in the patterns—note that even a tiny motion of the front will cause a narrow zone of black/white contrast right at the edge of the front (and is indeed obtained, if p_{CO} conditions are adjusted which induce this

Island growth during CO oxidation / Pt(111)

pumping speed = 85 l/s

 $p_{O_2} = 4 \times 10^{-4}$ Torr

T = 413.2 K

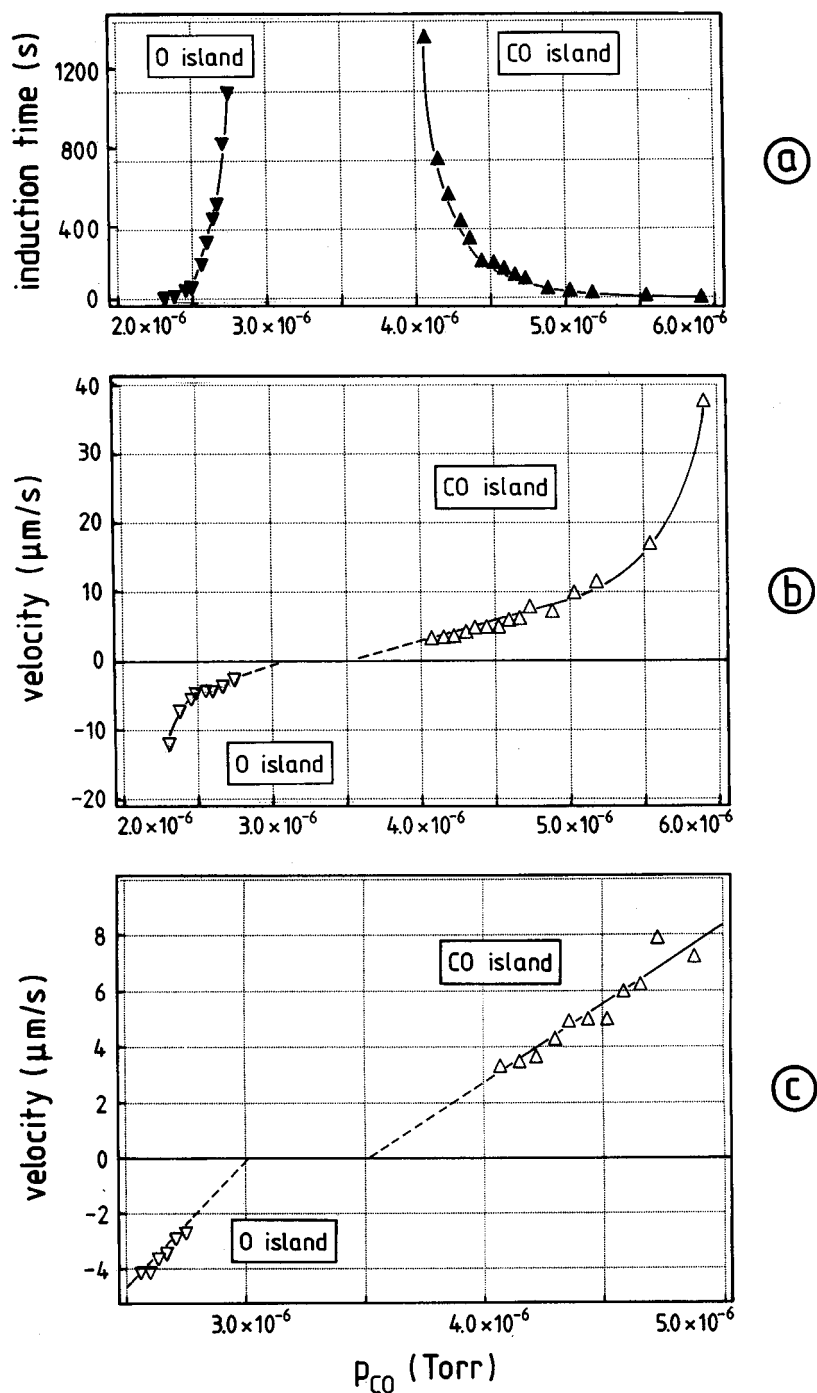


FIG. 13. *Upper panel:* Induction times observed during the growth of oxygen and CO islands, as a function of the CO partial pressure. There is a pressure interval ($\sim 3 \times 10^{-6} \leq p_{CO} \leq 4 \times 10^{-6}$ Torr) in which extremely long, possibly infinitely long, induction times occur. *Middle panel:* Plot of the velocity of (island) front motion against the CO partial pressure. Note that the respective velocity of oxygen islands has been given a negative sign. *Bottom panel:* Enlargement of the middle panel in the pressure regime ($\sim 3 \times 10^{-6} \leq p_{CO} \leq 4 \times 10^{-6}$ Torr) showing the discontinuity in the growth rate of the islands which we interpret as proof for the existence of an experimental bistable region.

motion). Slight changes of the decisive CO partial pressure do not noticeably alter this situation as long as p_{CO} is strictly kept within the above pressure limits. However, small CO pressure changes performed in the region of experimental bistability make the front move for a certain time period, thereafter, it stops again and is absolutely stable, at least as long as the CO pressure remains constant. This slight motion

makes it difficult to determine the border of the interval with $\nu=0$ exactly.

These results demonstrate also the very low level of intrinsic and technical noise in the system on the mesoscopic level. It is just this absence of a veil of dense noise that enables us to locate the finite interval of CO-partial pressures which make the reaction/diffusion front stop. Note that the

respective experiments are by no means trivial, since it is necessary to keep all external control parameters (F, T , partial pressures) *absolutely constant* over such a long time period. As soon as p_{CO} (or any other parameter) runs out of the range, the islands either shrink or expand, and the whole system inevitably moves either to the oxygen side {1} or to the CO side {3}. The different CO partial pressures at ν_A and ν_B (which determine the width of the experimental bistable region) can be estimated from the fact that they cause a vanishing front velocity of the islands. We may put this result differently and state that it indicates a clear, *real* hysteresis, because *there exist two stable steady states in the experimental bistable region*. Accordingly, we regard our finding as the first evidence of a stable hysteresis occurring in the catalytic CO oxidation on a Pt single-crystal surface. In addition, this result may have an impact for heterogeneous surface reactions in general! Note that the theoretical considerations of Zhdanov and Kasemo²⁴ and Bär *et al.*²⁷ rather predict a single equistability point η [=single-valued CO partial pressure, cf. Fig. 1(b)] at which the island growth rate slows down to zero, while we find an obviously *extended* p_{CO} range for this condition. In regard to the principle reaction diagram shown in Fig. 1(c), we supply herewith the experimental basis for the construction of the S-shaped curve. We call the region in which the velocity of the reaction/diffusion front remains zero, the “experimental bistable region,” and the corresponding hysteresis a “*true or real* hysteresis.” The experimental bistable region therefore is a subregion of the aforementioned region of assisted nucleation (computed bistable region). However, we would like to point out that the statement of Zhdanov and Kasemo²⁴ concerning the vanishing hysteresis is certainly correct, when the system suffers from a rather high noise level (which is unfortunately often the case). Then the aforementioned veil of noise will prevent the observation of the fine structure of the computed bistable region, especially close to the equistability point η .

We add that the measured induction times underlying our statement (cf., Figs. 12 and 13) are very reproducible and respond to changes of the CO partial pressure in a very predictable manner. If the same experiment is repeated several times the resulting overall PEEM photocurrent is practically identical. This means that statistical errors can be safely excluded. Furthermore, it is possible (for a given set of external control parameters) to make the reaction/diffusion fronts (the phase boundaries between CO and oxygen-covered surface areas) either stop or move back and forth in a well-defined manner simply by admitting a certain CO partial pressure to the reactor. It is really convincing to watch the motion of the respective fronts on the PEEM screen and their direct response to the CO pressure adjustment.

Finally, we would like to make another point: Unlike CO oxidation over Pt(100), (110), or (210) surfaces we *never succeeded in observing spatiotemporal oscillations* (spirals, target patterns, standing waves) on Pt(111) during cyclic variation of the CO pressure for otherwise constant external control parameters. The only observable features were nucleation of small patches and large islands, growth and shrinking, respectively, of CO and oxygen islands and stationary fronts as described above.

3. Isothermal front propagation and the role of defects

We move a step further and investigate possible reasons why the reaction fronts stop at certain CO partial pressures and give rise to the observed hysteresis. We have already mentioned the crucial role of surface defects and recall that the assisted nucleation of both CO and oxygen islands is apparently closely tied to certain defects on the surface (cf. Figs. 9 and 11). It is, therefore, a tempting experiment to make a reaction/diffusion front move (by adjusting a certain CO pressure), hit an “active” defect, and watch possible changes of its expansion velocity. An example is provided by Fig. 14. The CO pressure is adjusted in a way that the system is outside the experimental bistable region (which ensures that the islands grow and reaction/diffusion fronts move). The first two images, Figs. 14(1a) and 14(1b) show a CO front (which is more or less smooth on the mesoscopic scale) moving slowly to 2 o'clock direction [Fig. 14(1d)]. Inside the bright CO island one realizes some black spots which we associate with large surface defects (some of them are artificially colored for better orientation). That the defects play indeed a role in the front propagation can be deduced from Fig. 14(2a), in which the front motion has partially been retarded by a surface region with a high concentration of defects. The fronts develop further as is illustrated by Fig. 14(2) [note that the sample position has been shifted after images (1d) and (2a)]. Finally, the obstacles are overcome and the inhomogeneous shape of the front becomes smooth again.

We admit that these experiments are certainly too simple and somewhat ill-defined to reveal further details of the front propagation process. In particular, the atomistic “nature” of the defects cannot be judged from the PEEM measurements due to limited lateral resolution. Our observations simply prove that defects can at least retard, if not stop, the motion of reaction/diffusion fronts. This is known from many other (preferably PEEM) measurements in the recent literature.^{34,35} In Sec. IV, we will present preliminary results of simulations showing that a reaction/diffusion front can be retarded or even stopped at a line of defects, depending on the mutual distance of the obstacles. If intrinsic and technical fluctuations can be neglected, the interaction of reaction/diffusion fronts with local surface defects is a purely deterministic phenomenon which may be appropriately described by reaction/diffusion equations.

IV. DISCUSSION

In order to keep this discussion section as short and concise as possible we will expand on a few points only, all the more so since we have already given some basic information in Sec. I, whereby we refer especially to Fig. 1. We will particularly provide the reader with some results of simulations which may help to elucidate the role of “active” defects.

The most striking clue of our work is the experimental proof that a comparatively simple nonlinear reaction system exhibits a zone of “experimental bistability” inside the region of computed bistability determined by two bifurcations.

PEEM images of CO + O / Pt(111)

F (l/s)	p_{CO} (Torr)	p_{O_2} (Torr)	T (K)	Δt (s)
85	4.2×10^{-6}	4×10^{-4}	413.2	—

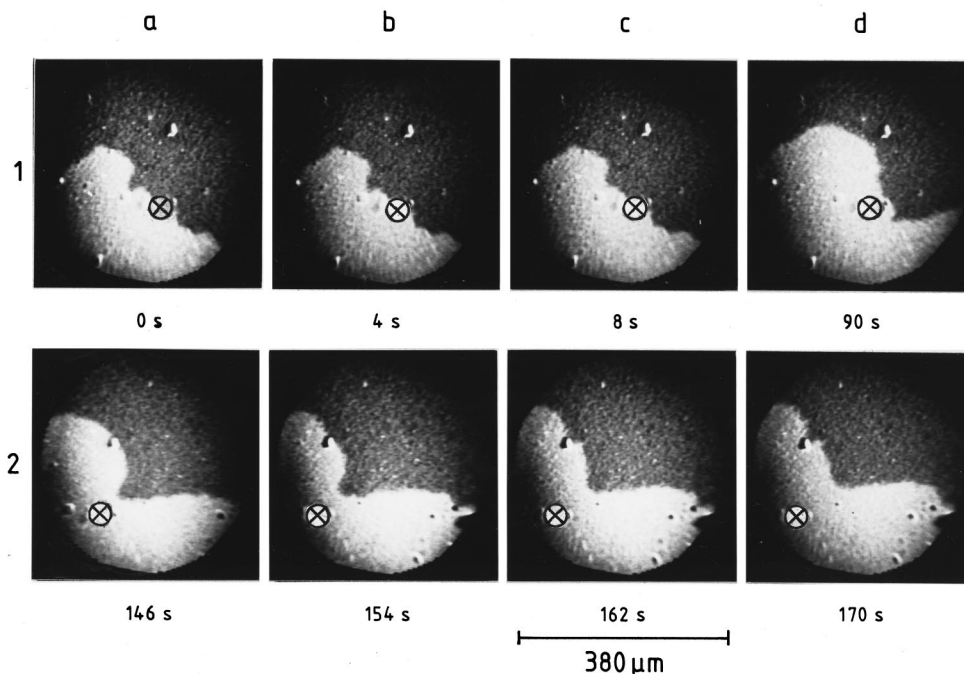


FIG. 14. Influence of surface defects on the front propagation as monitored by PEEM during the motion of a reaction/diffusion front. Some of the mesoscopic defects in the surface pin the reaction/diffusion process for a while, and the front velocity slows down. Finally the front passes the defect and becomes flatter again. Note that the sample position was shifted after images 1d and 2a and some defects were artificially marked for orientation.

Neither is this behavior predicted by current simulations based on the simple homogeneous level of the Langmuir–Hinshelwood model with diffusion terms excluded, nor by the more sophisticated heterogeneous level which considers diffusion processes. Our experimental results rather show that surface defects play a crucial role in that they can act as centers for nucleation (assisted nucleation of either CO or oxygen islands) or that they may impair or even stop the propagation of reaction/diffusion fronts. There is a (small) range of control parameter variation (in our case the CO partial pressure) in which either state of the system (reactive state=oxygen covered, nonreactive state=CO covered) is *stable*. The state of the system depends thereby on the history, i.e., from which monostable region A or B one approaches and enters the region of experimental bistability. We recall that this result is in contrast to theoretical predictions of Zhdanov and Kasemo,²⁴ who investigated the catalytic CO oxidation on a Pt(111) surface within the LH model and include diffusion terms, but neglected surface defects. They claim that only a single-valued CO pressure (equistability point η) separates the area of exclusive oxygen island growth from that of exclusive carbon monoxide island growth. Therefore a reaction system would inevitably transform between the steady state of high and low reactivity, if nucleation and growth of the respective islands are suffi-

ciently fast. Here we cannot help to note that the frequently quoted article by Zhdanov and Kasemo²⁴ is not based on results of a direct simulation which could confirm the authors' main conclusions.

A vast amount of previous (theoretical and experimental) studies focuses on the physical origin of spontaneous nucleation and pattern formation phenomena occurring during homogeneous reactions in solutions or in the course of heterogeneous surface reactions (as in our case).^{1,3,4,24} It is generally accepted that a so-called pacemaker plays a decisive role, a small region with parameters that differ from those of the bulk (for solution reactions) or the representative surface (for heterogeneous surface reactions).^{36,49} Recently Mikhailov³⁷ modeled a surface chemical reaction mesoscopically by including reaction/diffusion equations and concluded that spontaneous nucleation could come about by attractive lateral interactions between the reactive species. Another recent study by Bär *et al.*³⁸ modeled composite catalyst surfaces with “inert” and “active inclusions” and showed that spiral patterns and wave trains could evolve from these inclusions. (In previous experimental work by Graham *et al.*,^{39,40} “inclusions”—which are nothing else but artificial surface inhomogeneities—had been tailored by titanium squares (diameter $\sim 7 \mu\text{m}$) deposited onto a reactive Pt(110) surface and were shown by the PEEM method to

affect the formation and shape of reaction/diffusion fronts). In another work, Rose *et al.* could convincingly demonstrate by mirror electron microscopy that nucleation of chemical reaction fronts can and will take place at surface defects.⁴¹ Yet, quantitative structural or mechanistic information on this nucleation process was not available due to the still limited lateral resolution (of several μm only) of the respective microscopic experiments.

In our work, the role of defects or, more generally, surface inhomogeneities on the expansion and propagation of reaction/diffusion fronts was investigated. These inhomogeneities most likely consist of crystallographic perturbations, but may equally well involve active foreign surface atoms (carbon, for example). We learned from our PEEM measurements that certain “active” defects can strongly influence the expansion of a growing CO or oxygen island. This behavior is known for some time, and in order to pinpoint the peculiar role of the defects various simulations were performed in the past for equations of the $A+B_2$ type.⁴² Somewhat more sophisticated simulations thereby departed from the heterogeneous level of the LH model^{24,27} as described above. Motivated by our new findings which revealed that reaction/diffusion fronts could be stopped by control of the CO partial pressure we also use the heterogeneous level of simulation,^{24,27} but additionally include “active” defects which are able to “pin” reaction/diffusion fronts. While the outline of the theory as well as the body of results will be published in a forthcoming paper,⁴³ we give just a brief sketch of the considerations, but do not dwell upon theory here. The extended level of the LH model used in our simulations is expressed in the following nonlinear partial differential equations which consider the inhomogeneity of the surface explicitly. Local surface defects are represented by spatial subareas $\omega_i(x_1, x_2, I_1, I_2)$, $i=1,2,\dots$ with size I_1, I_2 , surrounding the center of inhomogeneity with coordinates x_1, x_2 :

$$\frac{\partial \theta_1}{\partial t} = \sum_{k=1}^2 \sum_{s=1}^2 \frac{\partial}{\partial x_k} \left\{ D_{k,s}(\theta_1, \theta_2, x_1, x_2) \frac{\partial \theta_s}{\partial x_k} \right\} + f_1(p_{\text{CO}}, \theta_1, \theta_2, x_1, x_2), \quad (1)$$

$$\frac{\partial \theta_2}{\partial t} = f_2(p_{\text{O}_2}, \theta_1, \theta_2, x_1, x_2), \quad (2)$$

$$\left. \frac{\partial \theta_i}{\partial n} \right|_{\partial \Omega(L_1, L_2)} = 0, \quad \theta_i(x_1, x_2, 0) = \theta_{0,i}(x_1, x_2) \quad \text{with } i=1,2. \quad (3)$$

The symbols have the following meaning:

$\Theta_1(x_1, x_2, t)$ and $\Theta_2(x_1, x_2, t)$ = surface coverages with CO and oxygen, respectively; x_1, x_2 = Cartesian coordinates of the point in the rectangle area $\Omega(L_1, L_2)$ with side length L_1 and L_2 , t = time, n = normal vector to the rectangle boundary $\partial \Omega(L_1, L_2)$, $D_{k,s}(\Theta_1, \Theta_2, x_1, x_2)$ = elements of diffusion matrix in xk direction, $f_1(p_{\text{CO}}, \Theta_1, \Theta_2, x_1, x_2)$ = rate of change in CO coverage, $f_2(p_{\text{O}_2}, \Theta_1, \Theta_2, x_1, x_2)$ = rate of change in oxygen coverage, $\Theta_{0,i}(x_1, x_2)$ = initial coverages of CO ($i=1$) and oxygen ($i=2$).

In principle, the defects or inhomogeneities could affect the heterogeneous reaction in various subtle ways, which are certainly difficult to model appropriately. We recall, however, that our experiments suggested a distinction between defects that are active in oxygen island formation and those that induce nucleation of CO islands. For the sake of simplicity, we define our “theoretical” defects only as follows: An “oxygen-type” defect provides a lower activation energy for desorption (=binding energy to the surface) of CO, and a “CO-type” defect exhibits a lower sticking coefficient for oxygen than the surrounding unperturbed surface area. Otherwise, the defect areas behave as the “nominal” surface defined by crystallography, in our case the Pt(111) surface.

The results of the respective simulations are reproduced in Figs. 15 and 16. The simulated images of Figs. 15 and 16 show the behavior of a moving reaction/diffusion front spreading across a surface with a kind of a barrier consisting of a line of seven hypothetical oxygen-type defects. Every such “image” is made up of 100×100 surface cells. The gray-level has been adjusted to model the surface coverage of CO and oxygen, respectively. According to our actual PEEM experiments we colored areas exhibiting high CO coverages bright and areas with a high oxygen coverage dark. The defects themselves are symbolized by white dots in the middle of each “image.” We initialize the computation in such a way that a stripe (10 cells wide) on the right border of the image is considered covered by CO, and all the rest of the image covered by oxygen. Thereafter, the external control parameter “CO pressure” is chosen in a way that an expansion of the CO stripe into the oxygen-covered surface region becomes possible; all other control parameters (the external ones being given in the legend to the figures) are kept constant.

Figure 15 illustrates the situation for a relatively high CO partial pressure. The CO front moves from right to left and gradually approaches the barrier line of oxygen-type defects. Apparently, they change the shape of the CO front and reduce its expansion velocity considerably. After a whole while, the front has overcome the defects, its borderline becomes flatter, and its original velocity is restored.

Figure 16 shows the behavior characteristic of a somewhat lower CO pressure ($p_{\text{CO}} = 3.15 \times 10^{-6}$ Torr). Again the CO front gradually moves from right to left and reaches the barrier of defects after approximately 150 s. Close to the line of “active” defects, the front slows down and becomes finally pinned [Fig. 16(2)]. This pinning can also be expressed in terms of a vanishing front velocity ($v=0$), and the important result of our simulation is that just the (oxygen-covered) surface part left of the line of defects will never become covered by CO. This inhibition of the motion of a CO front is not tied to a single, specific, CO partial pressure, but likewise occurs for a whole range of still lower CO partial pressures. We refer once again to Fig. 1(c) and state that the particular CO pressures at which the front velocity reaches zero are identified as the mesoscopic points ν_A and ν_B . Obviously our simulations reveal a region of bistability, which shows up in the experiment as a true macroscopic hysteresis, but only then, if “active” surface inhomogeneities are appropriately considered. The consequence is that

Computed images of CO+O / Pt(111)

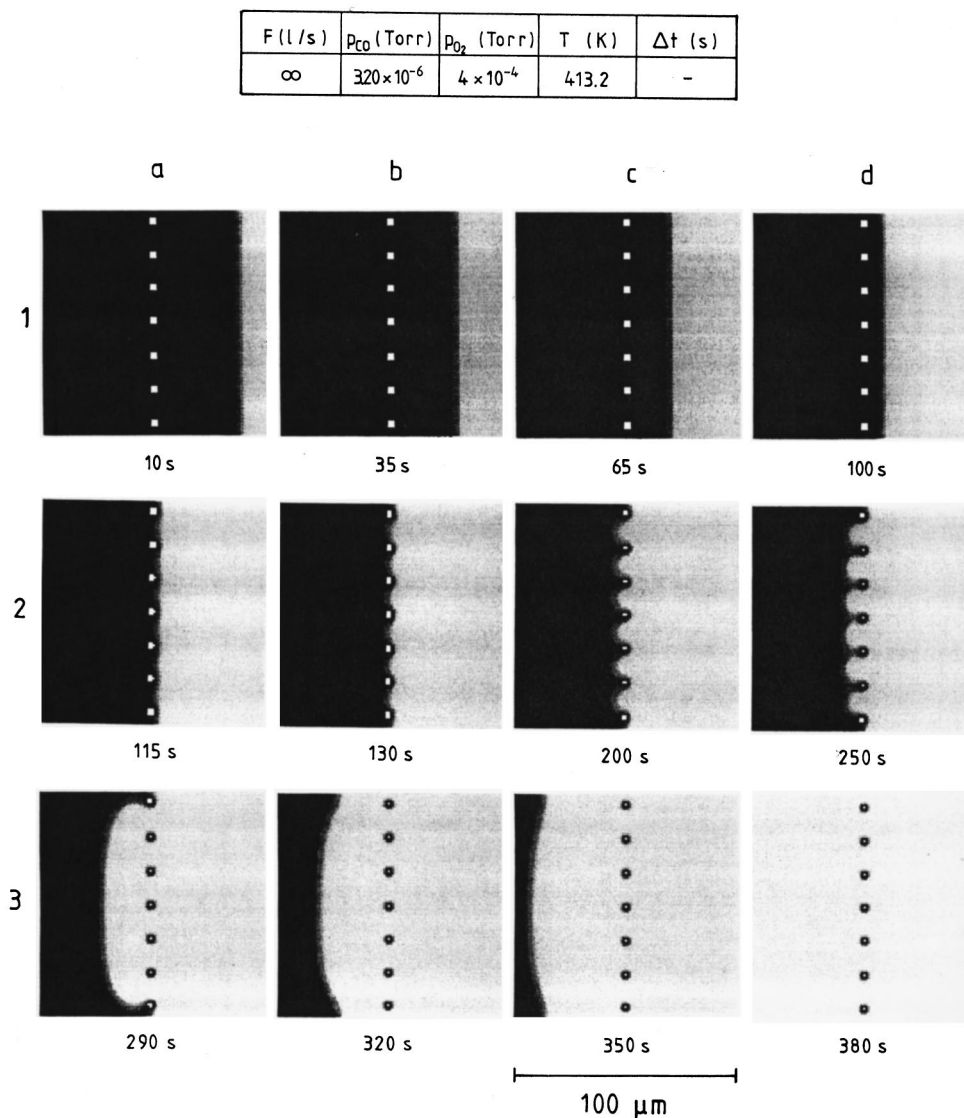


FIG. 15. Simulations of how a barrier of seven artificial oxygen-type defects influences the propagation of a CO front moving from right to the left in an initial oxygen environment. A relatively high CO pressure has been chosen in the simulation. The front is retarded, but not stopped by the barrier of defects.

for low noise level and in the presence of inhomogeneities heterogeneous (on surfaces) and homogeneous (in solutions) chemical reactions are realistically described by the S-shaped curve [Fig. 1(c)]!

In the foregoing sections we had expanded on the response of the reaction system to a variation of a single control parameter only, viz., the CO partial pressure. To discuss the properties of the system more generally, we must investigate also the role of various other control parameters such as the oxygen partial pressure and temperature. For this purpose, we recall the kinetic phase diagram representations of Figs. 3 and 4, spanned by the CO and oxygen partial pressure and surface temperature. In contrast to, e.g., a Pd(110) or Pt(210) surface, the kinetic phase diagram of the Pt(111) surface turns out to exhibit much less structure and may be regarded as a prototype of a comparatively simple dynamical system, at least within the parameter space investigated.

Both Pd(110) and Pt(210) exhibit fairly complicated cross-shaped phase diagrams which contain regions of temporal and spatiotemporal oscillations. For details, we refer to our previous work.^{12,18,44} Consequently, an observed hysteresis in the CO₂ formation rate changes its sense of rotation, and an isothermal cross-shaped phase diagram is obtained. In the case of Pt(111) surface a hysteresis is likewise observed, but it does not rotate with the oxygen pressure, i.e., the phase diagram is *not* of the cross-shaped type. According to Boissonade and de Kepper^{45,46} a cross-shaped phase diagram is a necessary condition for the occurrence of kinetic oscillations. Consistently, these oscillations were never found in the course of the catalytic CO oxidation on Pt(111), at least not in the parameter range covered in our experiments.

In our opinion the Pt(111) surface belongs to a class of systems that exhibit merely two monostable regions A and B separated by a region of bistability. Our data—the measure-

Computed images of CO+O / Pt(111)

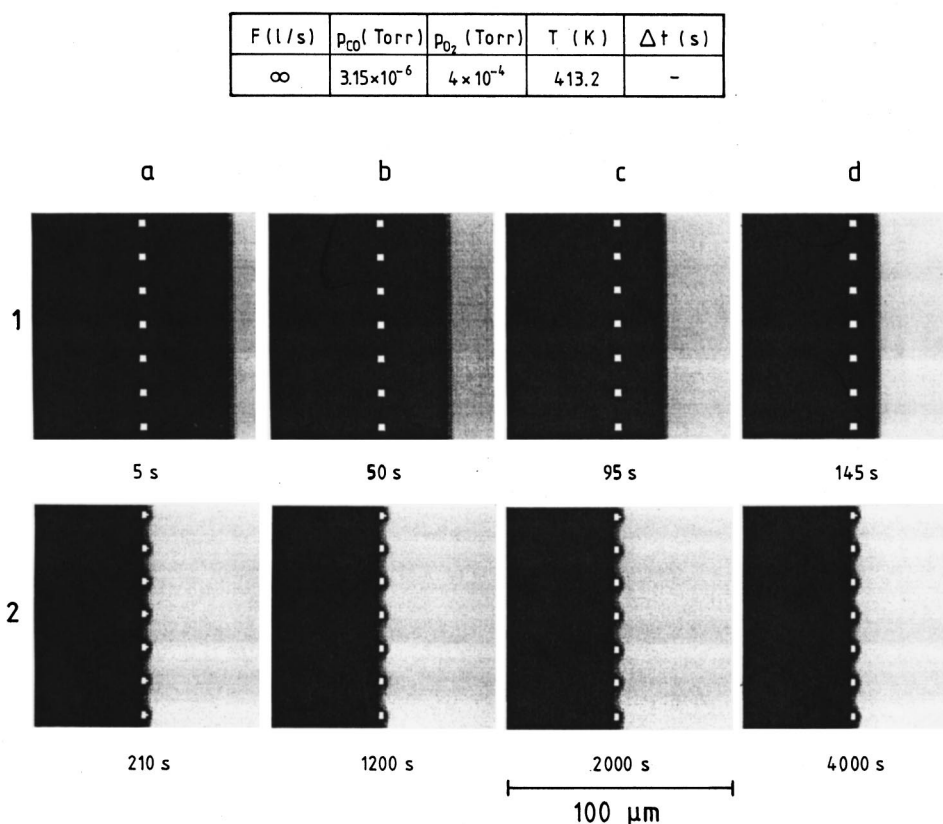


FIG. 16. Same situation as in Fig. 15 except that a smaller CO pressure was adjusted. This time the CO front is entirely stopped at the barrier, demonstrating that reaction/diffusion fronts can be pinned at defects, in agreement with experimental observations.

ments of the finite hysteresis loop as well as the vanishing front motion—clearly show that this bistable region really exists, i.e., the two phase boundaries ($\mu_{A,B}$): monostable region A \parallel (computed) bistable region \parallel monostable region B do not degenerate to a single equestability point η . Instead of this equestability point two further phase boundaries ($\nu_{A,B}$) appear inside the computed bistable region: assisted nucleation region of oxygen islands \parallel experimental bistable region \parallel assisted nucleation region of CO islands. Although our time-dependent measurements (which enable us to construct the aforementioned macroscopic kinetic phase diagrams) could not truly map the exact location of either *mesoscopic* points $\mu_{A,B}$ and $\nu_{A,B}$, the lines established by the *macroscopic* points $\tau_{A,B}$ at least indicate the parameter regions in which the mesoscopic points will occur.

Finally, we would like to point to some further experimental and theoretical work that might support our conclusions. Stokes *et al.*⁵⁰ report about pinning of an interface between two immiscible liquids (water and decane) in a porous tube. This interface moves under the operation of a pressure difference between both ends of the tube but becomes pinned in a certain region of this pressure difference ($\nu=0$). Outside this *pinning region* the interface moves in proportion to the pressure difference, thus providing an interesting similarity to our results presented in Fig. 13(c). Inside the pinning region the interface motion gradually slows

down to a velocity of zero. Stokes *et al.* conclude that the interface may be pinned at microscopic heterogeneities present in the surface of the pores. In a theoretical work Ebeling *et al.*⁵¹ consider the influence of static and dynamic inhomogeneities (disorder) on the formation of structure and on the propagation of fronts in a reaction/diffusion system. They find that the velocity of a front will move with a velocity that is locally different, because its propagation may be hindered or even stopped by disorder (similar to the situation displayed in our Fig. 14). Similar conclusions, namely a pinning of a two-dimensional front, are arrived at by Koplík and Levine.⁵²

It would be quite interesting and possibly revealing to study other heterogeneous dynamic reaction systems whether or not the computed bistable region may contain a subregion of experimental bistability. Among others, the very direct response of the motion of a reaction/diffusion front on the adjustment of an external control parameter may provide a kind of a “chemical switch” which can be used to control the optical or electrical properties of a macroscopic surface. On the other hand, artificial inhomogeneities like deposited foreign atoms may allow to stabilize the steady state of high reactivity by shifting the point ν_A and to obtain a higher production yield in reactions with technical catalysts.

ACKNOWLEDGMENTS

The authors gratefully acknowledge support from the DFG (through SFB 290) and the Fonds der Chemischen Industrie. The work was also partially supported by the Russian Fund of Fundamental Research (Grant No. 96-01-00812) and INTAS 95-186. We thank Professor Bernhard Delmon/Belgium for his special assistance and Dr. K.-P. Charlé for helpful discussions.

- ¹ *Oscillations and Traveling Waves in Chemical Systems*, edited by R. J. Field and M. Burger (Wiley, New York, 1985).
- ² *Complex Chemical Reaction Systems (Mathematical Modeling and Simulation)*, Springer Series in Chemical Physics Vol. 47, edited by J. Warnatz and W. Jäger (Springer, Berlin, 1987).
- ³ G. Nicolis and I. Prigogine, *Self-Organization in Nonequilibrium Systems, From Dissipative Structures to Order through Fluctuations* (Wiley, New York, 1977).
- ⁴ A. Babloyantz, *Molecules, Dynamics and Life—An Introduction to Self-Organization of Matter* (Wiley, New York, 1986).
- ⁵ P. B. Belousov, *Khim. Zhizn.* **7**, 65 (1982).
- ⁶ A. M. Zhabotinskii and A. N. Zaikin, in *Oscillating Processes in Biological and Chemical System II*, edited by E. E. Sel'kov (Nauka, Puschino, 1971), p. 279.
- ⁷ (a) R. Imbihl and G. Ertl, *Chem. Rev.* **95**, 697 (1995); (b) R. Imbihl, *Prog. Surf. Sci.* **44**, 185 (1993).
- ⁸ G. Ertl, *Ber. Bunsenges. Phys. Chem.* **90**, 284 (1986).
- ⁹ (a) R. Imbihl, M. P. Cox, and G. Ertl, *J. Chem. Phys.* **84**, 3519 (1986); (b) R. Imbihl, M. P. Cox, G. Ertl, H. Müller, and W. Brenig, *ibid.* **83**, 1578 (1985).
- ¹⁰ S. Nettesheim, A. von Oertzen, H. H. Rotermund, and G. Ertl, *J. Chem. Phys.* **98**, 9977 (1993).
- ¹¹ (a) G. Haas, R. U. Franz, H. H. Rotermund, R. M. Tromp, and G. Ertl, *Surf. Sci.* **352–354**, 1003 (1995); (b) H. H. Rotermund, G. Haas, R. U. Franz, R. M. Tromp, and G. Ertl, *Science* **270**, 608 (1995).
- ¹² M. Berdau, A. Karpowicz, G. G. Yelenin, K. Christmann, and J. H. Block, *J. Chem. Phys.* **106**, 4291 (1997).
- ¹³ H. H. Rotermund, W. Engel, M. Kordesch, and G. Ertl, *Nature (London)* **343**, 355 (1990).
- ¹⁴ M. Eiswirth and G. Ertl, *Surf. Sci.* **177**, 90 (1986).
- ¹⁵ M. Eiswirth, K. Krischer, and G. Ertl, *Surf. Sci.* **202**, 565 (1988).
- ¹⁶ M. Ehsasi, S. Rezaie-Serej, J. H. Block, and K. Christmann, *J. Chem. Phys.* **92**, 7596 (1990).
- ¹⁷ M. Ehsasi, A. Karpowicz, M. Berdau, W. Engel, K. Christmann, and J. H. Block, *Ultramicroscopy* **49**, 318 (1993).
- ¹⁸ M. Ehsasi, M. Berdau, T. Rebitzki, K.-P. Charlé, K. Christmann, and J. H. Block, *J. Chem. Phys.* **98**, 9177 (1993).
- ¹⁹ G. Veser, P. A. Thiel, and R. Imbihl, *J. Chem. Phys.* **98**, 2148 (1994).
- ²⁰ G. Veser and R. Imbihl, *J. Chem. Phys.* **100**, 8483 (1994).
- ²¹ L. F. Razon and R. A. Schmitz, *Catal. Rev. Sci. Eng.* **28**, 89 (1986).
- ²² G. Ertl, *Adv. Catal. Rel. Subj.* **37**, 213 (1990).
- ²³ F. Schüth, B. E. Henry, and L. D. Schmidt, *Adv. Catal.* **39**, 51 (1993).
- ²⁴ V. P. Zhdanov and B. Kasemo, *Surf. Sci. Rep.* **20**, 111 (1994).
- ²⁵ K. Christmann, *Introduction to Surface Physical Chemistry* (Steinkopff, Darmstadt, 1991).
- ²⁶ R. M. Ziff, E. Gulari, and Y. Barshad, *Phys. Rev. Lett.* **56**, 2553 (1986).
- ²⁷ M. Bär, Ch. Zülicke, M. Eiswirth, and G. Ertl, *J. Chem. Phys.* **96**, 8595 (1992).
- ²⁸ W. Engel, M. E. Kordesch, H. H. Rotermund, S. Kubala, and A. von Oertzen, *Ultramicroscopy* **36**, 148 (1991).
- ²⁹ G. N. Derry and P. N. Ross, *J. Chem. Phys.* **82**, 2772 (1985).
- ³⁰ (a) G. Ertl, M. Neumann, and K. M. Streit, *Surf. Sci.* **64**, 393 (1977); (b) P. R. Norton, J. W. Goodale, E. B. Selkirk, *ibid.* **83**, 189 (1979).
- ³¹ F. Schlögl, *Z. Phys.* **248**, 446 (1971); **253**, 147 (1972).
- ³² M. Mundschau, M. E. Kordesch, B. Rausenberger, W. Engel, A. M. Bradshaw, and E. Zeitler, *Surf. Sci.* **227**, 246 (1990).
- ³³ W. Swiech, B. Rausenberger, W. Engel, A. M. Bradshaw, and E. Zeitler, *Surf. Sci.* **294**, 297 (1993).
- ³⁴ J. Maselko and K. Showalter, *Physica D* **49**, 21 (1991).
- ³⁵ G. Haas, M. Bär, I. G. Kevrekidis, P. B. Rasmussen, H. H. Rotermund, and G. Ertl, *Phys. Rev. Lett.* **75**, 3560 (1995).
- ³⁶ J. J. Tyson and P. C. Fife, *J. Chem. Phys.* **73**, 2224 (1980).
- ³⁷ M. Hildebrandt and A. S. Mikhailov, *J. Phys. Chem.* **100**, 19089 (1996).
- ³⁸ M. Bär, A. K. Bangia, I. Kevrekidis, G. Haas, H. H. Rotermund, and G. Ertl, *J. Phys. Chem.* **100**, 19106 (1996).
- ³⁹ M. Graham, I. G. Kevrekidis, K. Asakura, J. Lauterbach, K. Krischer, H. H. Rotermund, and G. Ertl, *Science* **264**, 80 (1994).
- ⁴⁰ M. Graham, M. Bär, I. G. Kevrekidis, K. Asakura, J. Lauterbach, H. H. Rotermund, and G. Ertl, *Phys. Rev. B* **52**, 76 (1995).
- ⁴¹ K. C. Rose, R. Imbihl, B. Rausenberger, C. S. Rastomjee, W. Engel, and A. M. Bradshaw, *Surf. Sci.* **352–354**, 258 (1996).
- ⁴² J. Mai and W. von Niessen, *J. Chem. Phys.* **98**, 2032 (1993).
- ⁴³ G. G. Yelenin *et al.* (unpublished).
- ⁴⁴ M. Ehsasi, C. Seidel, H. Ruppender, W. Drachsel, J. H. Block, and K. Christmann, *Surf. Sci.* **210**, L198 (1989).
- ⁴⁵ J. Boissonade and P. de Kepper, *J. Phys. Chem.* **84**, 501 (1980).
- ⁴⁶ P. de Kepper and J. Boissonade, in *Oscillations and Traveling Waves in Chemical Systems*, edited by R. J. Field and M. Burger (Wiley, New York, 1985), Chap. 7.
- ⁴⁷ M. Ehsasi, M. Matloch, O. Frank, J. H. Block, K. Christmann, F. S. Rys, and W. Hirschwald, *J. Chem. Phys.* **91**, 4949 (1989).
- ⁴⁸ V. P. Zhdanov, *Phys. Rev. E* **50**, 760 (1994).
- ⁴⁹ G. G. Yelenin and A. G. Makeev, *Mathematical Modelling* (1996), Vol. 8, N12, pp. 62–76.
- ⁵⁰ J. P. Stokes, A. P. Kushnick, and M. O. Robbins, *Phys. Rev. Lett.* **60**, 1386 (1988).
- ⁵¹ W. Ebeling, A. Engel, L. Schimansky-Geier, and Ch. Zülicke, *Physica D* **49**, 170 (1991).
- ⁵² J. Koplik and H. Levine, *Phys. Rev. B* **32**, 280 (1985).